Original Article

Author for correspondence:
Adam J. Cawood,
Email: adam.cawood@swri.org

Mineralogy controls fracture containment in mechanically layered carbonates

Nina P. Bowness, Adam J. Cawood ⬤, David A. Ferrill, Kevin J. Smart and Harrison B. Bellow

Southwest Research Institute, 6220 Culebra Road, San Antonio, Texas 78238-5166, USA

Abstract

Understanding the distribution and geometry of faults and fractures is critical for predicting both subsurface permeability architecture and the integrity of geological fluid barriers, particularly in rocks with low primary porosity and permeability. While fracture patterns in relatively competent, weathering-resistant (therefore often well-exposed) rocks are generally well studied in outcrop, the role of mechanically weak layers in defining fracture patterns is frequently overlooked or under-represented. Here we show that rock composition, specifically clay and silicate minerals versus carbonate content, exerts a strong control on fault and fracture propagation and bed-containment within a mechanically layered, Cretaceous carbonate sequence at Canyon Lake Gorge, Texas. We find that relatively incompetent, clay-rich layers limit fault and fracture propagation, and cause bed-containment of fractures in more competent beds. In our results, no clear relationships exist between mechanical layer thickness and fracture abundance. These results are important for understanding the relative importance of composition versus bed thickness on fracture abundance in the subsurface, and for predicting fracture-controlled fluid flow pathways, seals and fracture connectivity across beds with variable compositions, thicknesses and competences.

1. Introduction

Subsurface flow pathways are vital for geothermal energy production (e.g. Gan & Elsworth, 2014), aquifer recharge and connectivity (e.g. Bauer *et al.* 2016) and hydrocarbon extraction (e.g. Fisher & Knipe, 2001). Conversely, geological barriers or baffles to fluid flow are necessary for sustainable and long-term disposal of hazardous waste (e.g. Gautschi, 2001) and carbon dioxide sequestration (e.g. Vialle *et al.* 2018) in the subsurface. Permeability in low-porosity carbonate rocks is primarily controlled by faults and fractures (e.g. Lattman & Parizek, 1964; Ferrill *et al.* 2012*a*, 2020*b*; Bisdom *et al.* 2017), but adequate sampling of these structures in the subsurface remains problematic. Borehole data can provide detailed information about fracture networks in the subsurface (e.g. Cooper, 1991), but predicting fracture patterns away from wells is challenging (e.g. De Marsily, 2005; Hooker *et al.* 2014; McGinnis *et al.* 2015). Where faults and fractures are resolvable in seismic data, only the largest structures in a given population are imaged (e.g. Yielding *et al.* 1996; Rawnsley *et al.* 2007; Worthington & Lubbe, 2007), and therefore the contribution of sub-seismic faults and fractures to permeability structure is often poorly constrained (Morris *et al.* 2009*a*).

Outcrop-based approaches to fracture characterization (e.g. Brenner & Gudmundsson, 2004; Ferrill & Morris, 2008; Hooker *et al.* 2013; McGinnis *et al.* 2015; Cilona *et al.* 2016; Laubach *et al.* 2018) may circumvent some of the challenges related to subsurface sampling, provided that applicable outcrop analogues and sampling strategies are chosen. Outcrop studies have shown that fracture patterns in multilayer systems can vary according to structural (e.g. Price, 1966; Stearns & Friedman, 1972; Hancock, 1985; Nelson, 2001; Morris *et al.* 2014) and stratigraphic factors (e.g. Rijken & Cooke, 2001; Ferrill & Morris, 2003*a,b*; Laubach *et al.* 2009; Ferrill *et al.* 2014). Documented controls on fracture abundance (spacing, density or intensity) include bed thickness (e.g. Harris *et al.* 1960, Price, 1966; McQuillan, 1973; Ladeira & Price, 1981; Corbett *et al.* 1987; Huang & Angelier, 1989; Narr & Suppe, 1991; McGinnis *et al.* 2017), grain size (Gasparrini *et al.* 2021), mechanical layer thickness (e.g. Gross, 1993), apparent rock strength (e.g. Price, 1966; Clarke & Burbank, 2011; Ferrill *et al.* 2014; McGinnis *et al.* 2017), subcritical crack growth (Atkinson, 1984; Schultz, 2000; Olson, 2004), structural position (e.g. Price, 1966; Stearns & Friedman, 1972; Zahm & Hennings, 2009; Morris *et al.* 2014), fracture cementation (Hooker *et al.* 2013; Hooker & Katz, 2015) and rock composition (e.g. Handin *et al.* 1963; Nelson, 2001). Previous studies have also investigated the relationship between mechanical stratigraphy and fracture stratigraphy. They reveal that while fracture stratigraphy reflects the mechanical stratigraphy during failure, mechanical properties change over time and therefore progressive diagenesis of the rock should be considered (Laubach *et al.* 2009).

While systematic relationships between fracture patterns and structural or stratigraphic factors have been documented in a number of cases, studies have also shown that systematic relationships are not always identifiable (e.g. McQuillan, 1973; Lamarche *et al.* 2012; McGinnis *et al.* 2015). The mechanical strength of rock layers, layer thickness and layer interfaces in sedimentary successions (collectively referred to as 'mechanical stratigraphy') have been shown to be an important factor in controlling fracture containment, vertical persistence (Stowell, 2001) and the likelihood for fractures to propagate across multiple layers (e.g. Gillespie *et al.* 2001; Ferrill & Morris, 2008; McGinnis *et al.* 2017; Douma *et al.* 2019). Where layer interfaces are weak or intervals between competent beds have low stiffness (e.g. low Young's modulus), fractures are less likely to propagate across layers (e.g. Corbett *et al.* 1987; Lorenz *et al.* 2002; Bourne, 2003; Ferrill *et al.* 2014; Giorgetti *et al.* 2016; Na *et al.* 2017). Bed-contained fractures in competent rock layers may therefore exhibit variable patterns from bed to bed (or between exposed bedding pavements), as previously documented at Canyon Lake Gorge, Texas (McGinnis *et al.* 2015).

The purpose of this study is to assess how relatively incompetent beds and weak bed interfaces influence fracture containment within relatively competent beds and fracture propagation across sedimentary sequences. Incompetent lithologies are generally less resistant to weathering than competent strata (e.g. Ledbetter Ferrill & Ferrill, 2021), and therefore outcrop-based fracture studies tend to focus on preferentially exposed competent units. Consequently, fracture patterns in relatively weak, weathered interbeds are less extensively characterized. Here we assess fault and fracture patterns in both competent and incompetent intervals in a carbonate succession by systematically sampling and mapping a series of interbedded packstone and wackestone units. Photogrammetric reconstruction, digital fracture mapping, compositional analysis, fracture intensity assessment and field data are used to characterize the role of mechanical stratigraphy on fault and fracture patterns. We show that unit and interface compositions are key controls on fault and fracture patterns, and that relatively minor bed-to-bed changes in clay content influence fracture propagation and containment. These findings have implications for predicting pathways, baffles and barriers for fluid flow in the subsurface, with applicability to groundwater management, hydrocarbon extraction, geothermal energy, and subsurface storage and sequestration.

2. Geologic background

Canyon Lake Gorge, located in the Balcones fault system of south-central Texas, provides an excellent exposure of the Hidden Valley fault zone, Cretaceous Glen Rose Formation carbonates and well-preserved fault and fracture networks (Fig. 1). The Balcones fault system formed in Oligocene–Miocene time to accommodate subsidence of the Gulf of Mexico basin margin (Ferrill *et al.* 2019 and references therein), and defines the transition between structurally stable flat-lying rocks of the Texas craton and the gently coastward-dipping sedimentary deposits of the Gulf of Mexico (Foley, 1926; Murray, 1961; Young, 1972; McGinnis *et al.* 2015). The Hidden Valley fault zone is 43–98 m wide with an average strike and dip of 057° and 67°, respectively (Ferrill *et al.* 2011; McGinnis *et al.* 2015). The exposed fault zone has provided a study area for numerous fault deformation analyses in mechanically layered carbonates for over two decades (e.g. Ferrill & Morris, 2008; Ferrill *et al.* 2008, 2009, 2011, 2012a, 2020a,b; Morris *et al.* 2009b; 2014) and analogues for deformation in mechanically layered reservoirs

regionally and around the world (e.g. Bodziak *et al.* 2014; Agar & Geiger, 2015; Solum & Huisman, 2017; Li *et al.* 2018). The fault and fracture networks exposed at Canyon Lake Gorge represent surface analogues for subsurface structures that may occur at depths (<5 km) typical for oil and gas reservoirs, CO_2 storage sites and groundwater aquifers. Specifically, the faults and fractures at Canyon Lake Gorge are direct analogues for groundwater flow pathways in the Glen Rose Formation in south Texas (M. A. Giles, unpub. M.S. thesis, Univ. Texas at San Antonio, 1992; Ferrill *et al.* 2008; McGinnis *et al.* 2015).

The rocks exposed in Canyon Lake Gorge are part of the Cretaceous Glen Rose Formation, the upper unit of the Trinity Group (Ward & Ward, 2007; Ferrill *et al.* 2011; Fig. 1). Both the upper and lower parts of the Glen Rose Formation are composed of cyclic depositional units on several scales, with the smallest scale cycles ranging from a few decimetres to 3 m thick (Ward & Ward, 2007; Ferrill *et al.* 2011). Lithologic units exposed in Canyon Lake Gorge include shallow water wackestone, packstone, grainstone, finely crystalline dolostone beds and a terrigenous claystone (Ward & Ward, 2007; Ferrill *et al.* 2011).

Approximately 5 m of the stratigraphic section is exposed across a series of stepped, bedding pavement surfaces at the study site, which is located in the northeastern part of Canyon Lake Gorge (Fig. 2). Fracture patterns in this area were assessed by McGinnis *et al.* (2015) through field-based fractured pavement mapping (see figs 1–3 in McGinnis *et al.* 2015). The authors found that fault and fracture patterns in the area exhibit variability in both orientation and areal intensity (total mapped fracture length per unit area) between exposed pavements, and that no direct relationship between bed thickness and fault or fracture frequency could be detected. We build upon the work of McGinnis *et al.* (2015) and extend their two-dimensional analyses of fracture patterns by (i) mapping fracture patterns in three dimensions across the study area, (ii) assessing vertical persistence of fractures through the exposure, and (iii) characterizing the influence of composition on fracture abundance and vertical persistence through the exposed carbonate succession at the site.

3. Methods and data

3.a. Lithological and mechanical stratigraphic characterization and compositional analysis

Twelve lithostratigraphic units are defined in this study (Fig. 3) based on outcrop morphology (weathering profile) and field observations of lithological variations through the exposed section. Lithological descriptions and interpretations of fossil assemblages in the study area were derived from field observations, photomicrograph interpretations and from the published lithostratigraphy of Canyon Lake Gorge (Ward & Ward, 2007; Ferrill *et al.* 2011). The previously published lithostratigraphy was modified and subdivided in the study area into 12 lithologic units (U1–U12). An N-type Schmidt hammer was used to measure the present-day, *in situ* elastic rebound of each lithologic unit at sample collection locations (see Fig. 2a for sampling locations) following the protocol of Morris *et al.* (2009b). Rebound data was used to characterize the relative stiffness of individual bedding layers and provides an approximation of rock strength. As noted by Morris *et al.* (2009b), Schmidt rebound values do not provide a direct measure of rock strength, but rather a proxy for present-day rock mechanical properties in outcrop (Katz *et al.* 2000; Aydin & Basu, 2005).
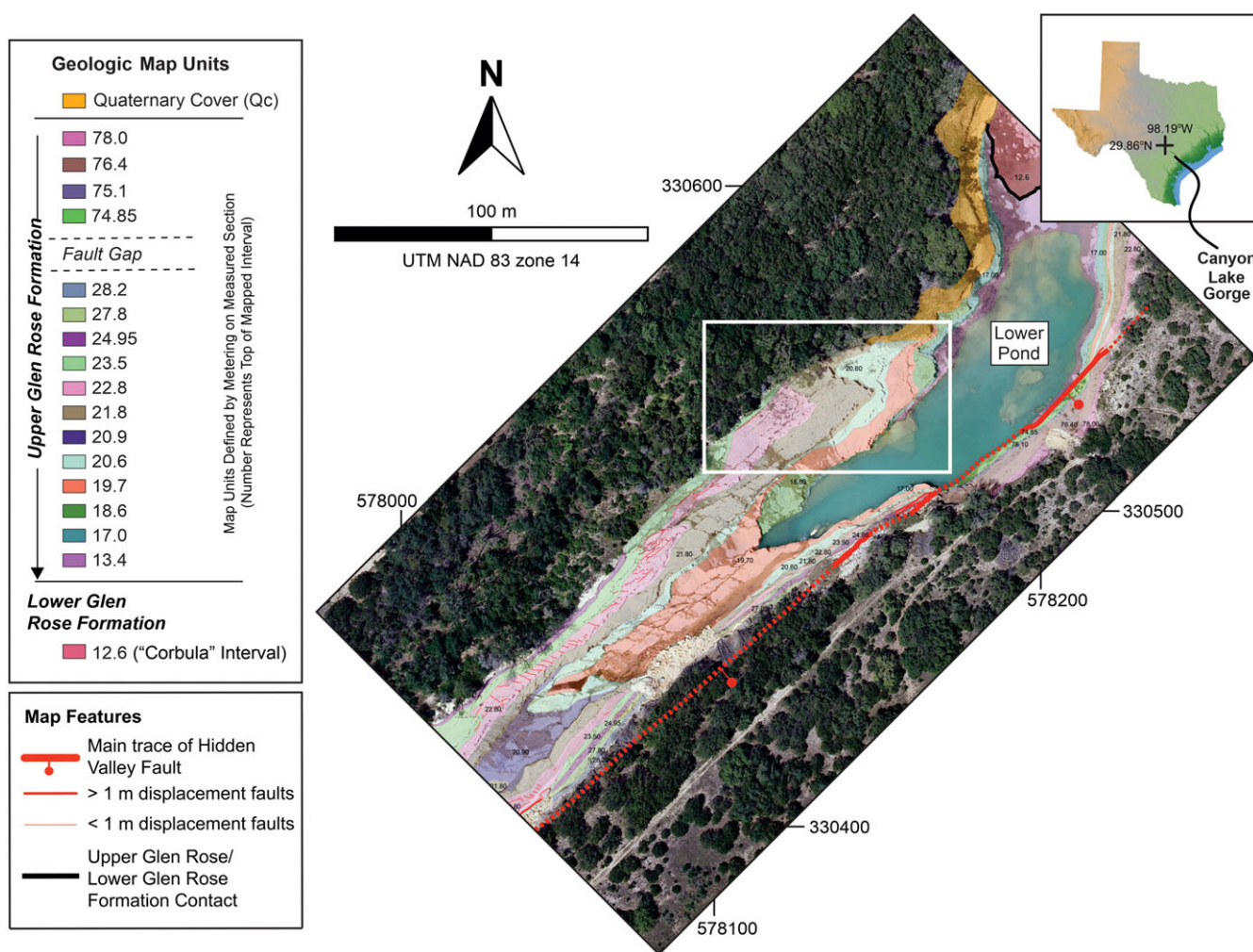
Fig. 1. Geologic map showing location of the study site (white outlined box) at Canyon Lake Gorge, Comal County, Texas. Map modified from Ferrill *et al.* (2011).

Samples from each of the 12 lithostratigraphic units (at sample locations mentioned above with Schmidt rebound data) were collected for X-ray diffraction (XRD) compositional analysis. Samples were analysed by Ryan King at Ellington Geological Services (Houston, Texas) for weight percentage of various minerals including quartz and feldspars, total clay and total carbonate. Samples were rinsed and air dried before being homogenized and crushed to <150 micron (100 mesh) prior to analysis. Bulk XRD was performed using a Bruker D2 Phaser. All diffraction patterns were hand-interpreted using the Reference Intensity Ratio (RIR) technique, MDI Jade software and PDF 4+ mineral diffraction database. Samples were then run through the D2 Phaser three times (as received, after 12 hours of glycolation and after heat treatment at 550 °C) to identify and quantify the clay species.

3.b. Field-based structural characterization

Faults in this study are defined as discrete fractures that exhibit either measurable displacement or visible evidence of slip in the form of slickenlines. Where brittle failure surfaces show no detectable evidence of either displacement or slickenlines, these surfaces were classified using the generic term 'fracture'. Non-fault fractures are subdivided into two categories based on their orientation with respect to bedding. 'High-angle fractures' have orientations that are >70° to bedding. 'Lower-angle fractures' have orientations that are <70° to bedding (Fig. 2). Where faults were measured in the field (shown by red dots in Fig. 2), fault orientations (strike and dip; using the right-hand rule where dip is to the right of the reported strike azimuth), fault slip directions (slickenline rake on the fault surface measured clockwise in the fault plane from the reported strike azimuth) and fault displacements parallel to fault plane slickenlines were measured by hand with a compass clinometer and folding ruler. The locations of faults measured in the field provided the basis for digital mapping and identification of faults where slickenlines could not be resolved in the photogrammetric reconstruction. Detailed observations of fault and fracture characteristics (e.g. terminations, linkage and morphology) were generally made in the field prior to subsequent digital interpretation of faults, fractures and bedding horizons.

3.c. Acquisition and processing of photogrammetry data

A total of 6300 aerial images were collected at the study site for subsequent photogrammetric reconstruction of the outcrop. Aerial photographs were acquired with a 24 mm focal length, 20 megapixel camera onboard a DJI Phantom 4 Pro unmanned
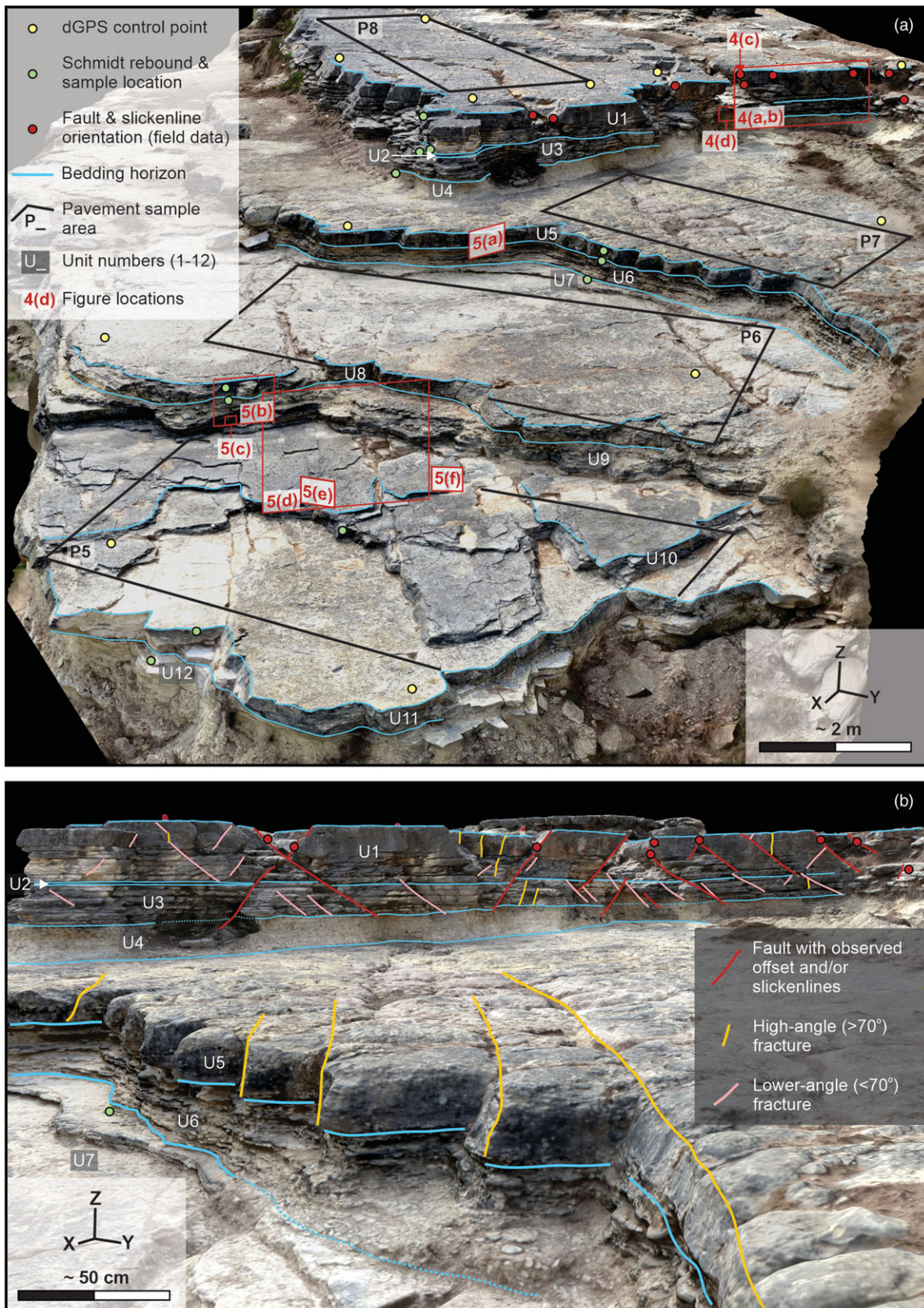
Fig. 2. Photogrammetric reconstruction of the study site in the northeastern part of Canyon Lake Gorge. (a) Summary bedding horizon interpretations, unit numbers, Schmidt rebound and sample locations, pavement sample areas, faults identified during fieldwork and locations of Figures 4 and 5. Direction of view is to the west. (b) Summary fault, fracture and bedding horizon interpretations on the photogrammetric reconstruction. Direction of view is to the southwest. Note that only a subsample of the fault and fracture population is shown for clarity. A 3D version of the photogrammetric reconstruction is available to view at https://bit.ly/3HHOLpm.
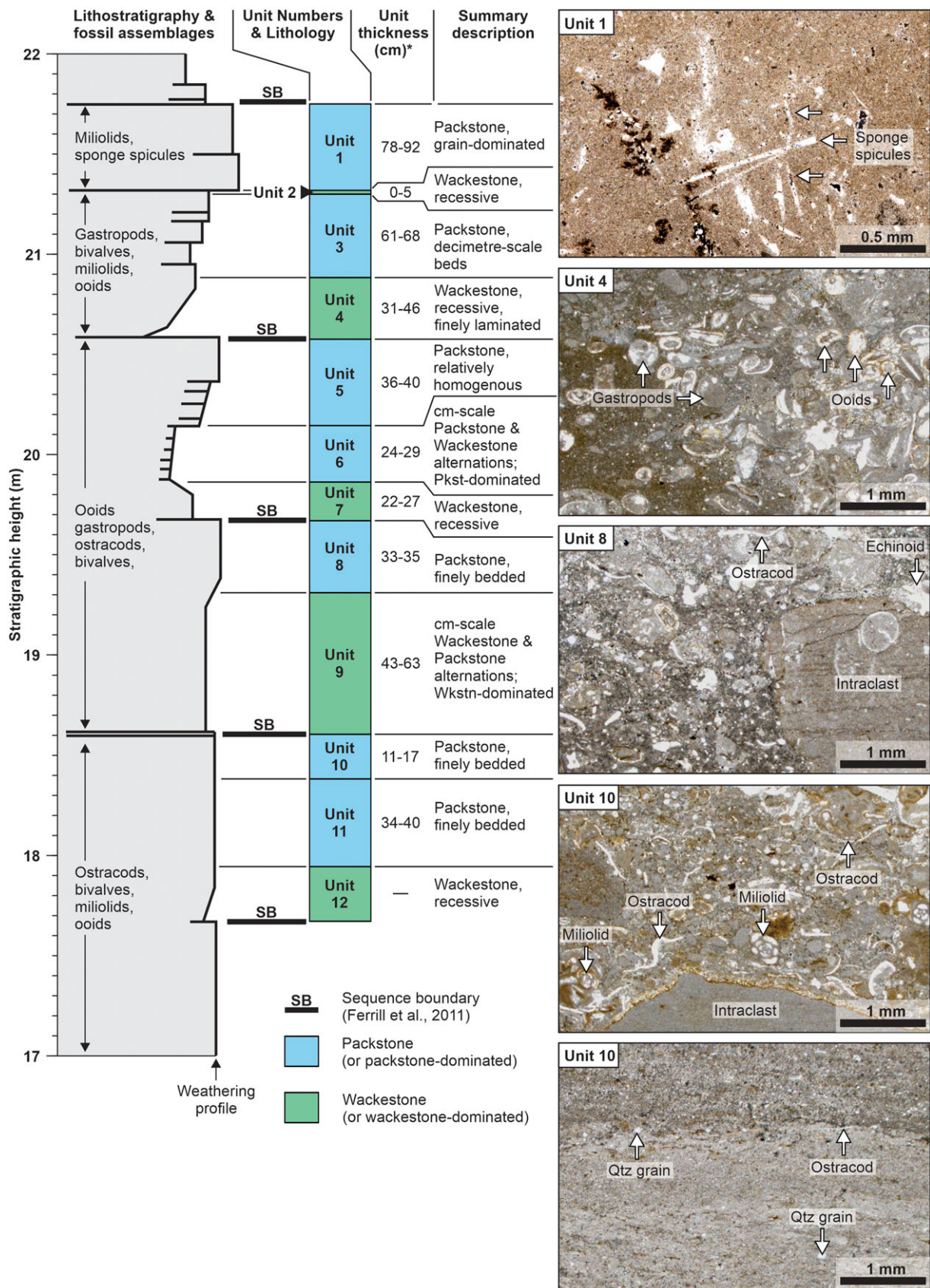
Fig. 3. Lithostratigraphic column with assigned unit numbers, measured interval thicknesses, summary descriptions of assigned units and photomicrographs showing fossil assemblages and sedimentary textures in Units 1, 4, 8 and 10. Lithostratigraphy and fossil assemblages modified from Ferrill *et al.* (2011). Unit thickness ranges shown were measured using projected polylines from mapping of the georeferenced photogrammetric reconstruction. Mismatches between measured thicknesses in this study and those represented by the modified lithostratigraphy of Ferrill *et al.* (2011) are attributed to lateral variations in unit thicknesses and thicknesses measured by Ferrill *et al.* (2011) being outside of our immediate study area.

aerial vehicle. Images were acquired using a fixed two-second interval shooting mode, a fixed ISO value of 400, variable shutter speeds and variable apertures. Image acquisition was carried out following established protocols (James & Robson, 2012; Cawood & Bond, 2018) to ensure sufficient overlap between images for photogrammetric reconstruction.

Digital reconstruction of the study site was achieved by aligning and processing aerial images using the digital photogrammetry structure-from-motion software Agisoft Metashape Professional (see Cawood *et al.* 2017 for details of photogrammetric processing steps). Image alignment and data processing yielded a dense point-cloud containing *c.* 14 million points, with an average point spacing of *c.* 9 mm over *c.* 1480 m^2. This point-cloud and a derived orthomosaic of 1.7 mm ground pixel resolution, also generated in Agisoft Metashape Professional, were used for subsequent interpretation and digitization of fracture traces and bed boundaries. Georeferencing of the outcrop reconstruction was achieved by surveying the positions of ground control points with a real-time kinematic differential global positional system (RTKDGPS). Fourteen ground control point locations (Fig. 2) were used to calibrate *x*, *y* and *z* point coordinates within the georeferenced point-cloud, and provided an estimated 12–15 mm absolute accuracy for the photogrammetric reconstruction and derived orthomosaic. In addition, accuracy of the photogrammetric reconstruction was assessed using previously published bed thickness measurements (McGinnis *et al.* 2015), as well as our own field measurements of bedding and fault surface orientations.

3.d. Fault and fracture digitization

Initial calibration of digital fault and fracture interpretations was achieved by comparing our results with previously published, field-mapping-derived pavement fracture maps of McGinnis *et al.* (2015). Digital fault and fracture interpretation of bedding pavements P5–P8 (using the pavement naming convention of McGinnis *et al.* 2015) was carried out in ArcMap 10.5.1 (ESRI) on the point-cloud-derived 2D orthomosaic of the study area (see Fig. 2 for pavement locations). Fracture digitization on the 2D orthomosaic was performed using a maximum zoom ratio of 1:3 to ensure that the orthomosaic was not too pixelated to discern details. Protocols for fracture mapping also included avoiding fracture digitization where pavement fracture traces were partially obscured by vegetation or debris. In cases where single fractures on bedding pavements hosted voids filled with dirt, debris or vegetation, fractures were digitized where visible along void edges to avoid interpreting fractures in zones with poor exposure.

Areal fault and fracture intensities (length per unit area) on bedding pavements were generated using the Line Density tool in ArcMap 10.5.1 (ESRI) with an output cell size of 0.05 m and a sampling circle with a radius of 0.5 m. The Line Density tool calculates fault or fracture intensity by dividing the summed length of digitized fracture traces within a sampling circle and divides that length by the circle area. Calculated fault or fracture intensity values are assigned to gridded raster cells, which in this case have dimensions of 0.05 m by 0.05 m. It should be noted that sampling circles and grid cells are not the same size. This results in overlapping sampling circles across the sampled domain. Three-dimensional interpretations of faults, fractures and bedding horizons on the photogrammetric reconstruction (see Fig. 2) were made using the 3D polyline tool in Agisoft Metashape Professional following similar protocols used during orthomosaic interpretation in 2D.

3.e. Cross-section construction and polyline projection

Subsequent to 3D digitization of fractures on the digital outcrop, the orientations of digitized faults and fractures were measured in CloudCompare (Girardeau-Montaut, 2011), and structures parallel or sub-parallel to the Hidden Valley fault were projected onto a digital cross-section for 2D analysis (see Cawood *et al.* 2022 for data projection protocols). Only the Hidden-Valley-fault-parallel faults and fractures (including those synthetic and antithetic to the Hidden Valley fault) were projected onto a cross-section in order to focus on the prevalent set of faults and fractures that trend parallel to the Hidden Valley fault, and to avoid orientation bias and the projection of structures not perpendicular to the projection plane. Fault, fracture and bed horizon polyline interpretations were projected to a cross-section oriented SSE–NNW (147°) in Move 2019.1^{TM} (Petroleum Experts Ltd.) using a projection vector perpendicular to the cross-section and parallel to the strike of the Hidden Valley fault (057°; Ferrill *et al.* 2011). Projected and resampled polyline interpretations were used to calculate 2D areas of lithologic units and cross-section lengths of projected faults and fractures within an interpretation boundary. This information was used to calculate average fracture intensity (total fracture length per unit area (m/m^2)) in cross-section for each of the assigned lithologic units.

4. Results

4.a. Lithostratigraphy and unit composition

Lithologies exposed at the study site (Fig. 1) include packstones, wackestones and thinly bedded intervals that we describe as packstone-dominated or wackestone-dominated (Fig. 3). Of the 12 lithologic units (U1–U12) assigned to the study area, five units (U2, U4, U7, U9, U12) are defined as wackestones or wackestone-dominated, and seven units (U1, U3, U5, U6, U8, U10, U11) are defined as packstones or packstone-dominated (Table 1). Bed thicknesses vary across relatively short distances (<10 m laterally) in all of the lithologic units (Fig. 3), and the Unit 2 wackestone shows thickness changes from a maximum of ~5 cm to an interpreted 0 cm, where this unit appears as a weathered (open) parting between Units 1 and 3. The weathering profile through the exposed strata in the study area (modified from Ferrill *et al.* 2011) shows an apparent, but not universal, relationship between lithology and resistance to weathering. Wackestone and wackestone-dominated intervals are generally more recessive and weathered than more competent packstone units. The exception to this general trend is where packstone-dominated intervals are characterized by centimetre-scale alternations between thicker packstone beds and thinner wackestone beds, despite being dominantly packstone (e.g. Unit 6; Fig. 3).

Fossil assemblages vary through the lithologic units, with ooids, gastropods, bivalves, ostracods, miliolids and sponge spicules present to varying degrees through Units 1–12 (Fig. 3). Composition and Schmidt rebound are variable through the exposed section (Table 1). The wackestone and wackestone-dominated Units 2, 4, 7, 9 and 12 have relatively high clay (6.61 to 9.88 %) and low carbonate (77.01 to 82.78 %) weight percentages, and relatively low average rebound values (9.6 to 14.1). Packstone and packstone-dominated Units 1, 3, 10 and 11 have relatively low clay (3.04 to 3.92 %) and high carbonate (87.72 to 89.33 %) weight percentages, and relatively high average rebound values (31.7 to 46.4). The packstone Units 5, 6 and 8 have higher clay (6.18 %, 6.32 %, 5.61 %) and lower carbonate (83.19 %, 82.03 %, 83.97 %)

Table 1. Lithology, average bed thickness, summary composition data, Schmidt rebound and summary fracture data for each of the 12 lithologic units

Bed ID	Lithology	Average bed thickness (m)	Total clay (wt %)	Quartz + feldspars (wt %)	Total carbonate (wt %)	Schmidt rebound mean	Fracture length (m) in cross-section	Bed area (m²) in cross-section	Calculated intensity (m/m²) in cross-section*
U1	Packstone	0.85	3.20	3.71	89.33	46.40	19.90	11.63	1.71
U2	Wackestone	0.025	6.61	6.63	82.78	11.70	–	0.14	–
U3	Packstone	0.65	3.43	5.03	87.75	41.90	19.02	8.42	2.26
U4	Wackestone-dominated	0.39	9.59	8.75	77.64	12.90	0.47	5.47	0.09
U5	Packstone-dominated	0.38	6.18	6.75	83.19	46.30	4.87	4.69	1.04
U6	Packstone-dominated	0.27	6.32	7.83	82.03	43.00	0.30	3.32	0.09
U7	Wackestone-dominated	0.25	8.42	10.57	77.01	9.60	0.01	3.18	0.00
U8	Packstone-dominated	0.34	5.61	6.62	83.97	39.10	2.39	3.17	0.75
U9	Wackestone	0.53	7.70	6.95	81.25	14.10	4.49	5.08	0.88
U10	Packstone	0.14	3.92	4.72	87.72	31.70	4.28	1.47	2.91
U11	Packstone	0.37	3.04	4.43	88.51	38.20	2.54	3.58	0.71
U12	Wackestone	–	9.88	8.47	78.36	10.30	–	–	–

*Note that fracture lengths and calculated fracture intensities are not provided for Unit 2 because of changes in unit thickness, and the potential for miscalculating unit areas and associated fracture intensities. The lower boundary of Unit 12 is poorly exposed and therefore bed thickness, bed area, and fracture lengths/intensities were not calculated for this unit.

weight percentages than the other packstone and packstone-dominated units, and high rebound (46.3, 43.0, 39.1) values (Table 1).

4.b. Structural observations

Brittle deformation in Units 1, 2 and 3 is dominated by normal faults (where offset or slickenlines were observed) and by lower-angle (<70° to bedding) fractures (where no visible offset or slickenlines are present). Most faults and lower-angle fractures in Units 1–3 exhibit similar orientations through vertical exposures of Units 1–3, dipping SSE and synthetic to the Hidden Valley fault, while some faults and lower-angle fractures dip in the opposite direction towards the NNW and antithetic to the Hidden Valley fault (Fig. 4a, b). High-angle fractures (>70° to bedding) are also present in Units 1–3, but these are relatively rare (Fig. 4b). No systematic abutting relationships are observed between lower-angle fractures and normal faults in Units 1, 2 and 3 (Fig. 4b). Intersections of high-angle fractures with lower-angle fractures are rare. The two high-angle fractures in Figure 4b terminate against a lower-angle fracture and a normal fault, indicating that the high-angle fractures formed after the lower-angle failure surfaces.

Fault surfaces identified in Units 1–3 record normal displacements of up to 15 cm (Table 2). In addition to visible offset, a number of the identified faults in Units 1–3 show evidence for slip in the form of slickenlines (Fig. 4c). These slickenlines record dominantly dip-slip motion along fault planes, with slickenline rakes of 78° to 90° (Table 2). Blocky calcite was identified adjacent to slickenlines on one fault plane in Unit 1 (Fig. 4c), which may be indicative of hybrid (combined tensile and shear) failure (Ferrill *et al.* 2012*a*, 2020*b,c*). Most faults and fractures present in Units 1–3 tend to persist for tens of centimetres across this interval but terminate at or within a few centimetres of the boundary between the Unit 3 packstone and

the underlying Unit 4 packstone (Figs 2b, 4b). Exceptions to this general trend, where lower-angle fractures or faults persist downwards by as much as 15 cm from the U3–U4 boundary, appear to be coincident with blockier zones in Unit 4, where this unit may locally contain more packstone (Fig. 4d). With the exception of occasional faults and fractures that terminate in the upper part of Unit 4, this interval is generally devoid of brittle deformation structures, particularly in the middle and lower parts of this unit.

No faults with visible offset or slip indicators are observed in the Unit 5 packstone. Deformation in this unit is dominated by regularly spaced, high-angle fractures that cross the entire vertical thickness (36–40 cm) of Unit 5. These high-angle fractures are exposed across Pavement 7, which is the bedding plane exposure of the U4–U5 interface (Fig. 2). The high-angle fractures in Unit 5 are strata-bound, and terminate at the U4–U5 boundary above and at the U5–U6 boundary below (Fig. 2b). Units 6 and 7, which are packstone and wackestone-dominated intervals, respectively, are both finely bedded, with centimetre-scale alternations between relatively competent and incompetent strata (Fig. 2b). A single, lower-angle mesoscale fracture is observed in Units 6 and 7, but otherwise no brittle failure surfaces are present in these intervals.

We document a single example of a normal fault zone that crosses multiple mechanical boundaries in Units 8 and 9 (Fig. 5a). This fault zone is represented by multiple fault strands with complex overlapping geometries, rather than by a single discrete fault surface (Fig. 5a). Brittle deformation structures are more common in the Unit 8 packstone and the wackestone-dominated Unit 9 compared to Units 6 and 7 above. High-angle fractures (Fig. 5b, d) and normal faults with up to 4 cm of displacement (Fig. 5b, c) are present in these units. High-angle fractures in Units 8 and 9 tend to be strata-bound, while observed normal faults cross unit interfaces (Fig. 5b). Two faults identified in Unit 9, with
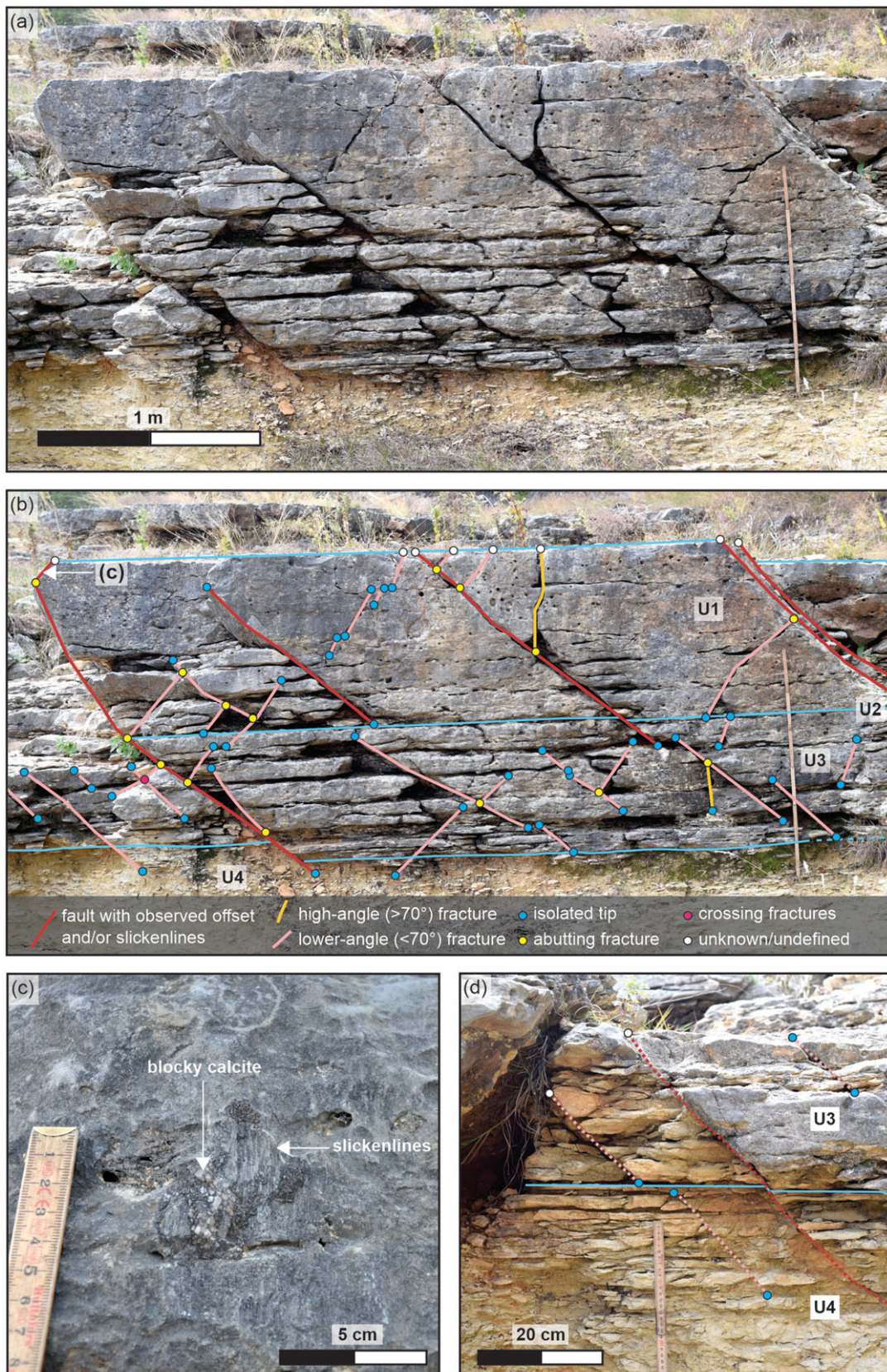
Fig. 4. (a) Field photograph showing vertical exposure of packstone beds U1 and U3, and underlying wackestone U4. (b) Annotated field photograph showing fracture abutting relationships and vertical penetration. (c) Slickenlines and blocky calcite on identified fault surface (location of fault surface shown in (b)). (d) Fractures and sub-parallel fault that are vertically persistent through the packstone unit but terminate within underlying wackestone unit. See Figure 2 for field photograph locations. Blue lines in (b) and (d) denote lithologic unit boundaries.

Table 2. Fault orientation and displacement data. Measurements acquired manually during fieldwork

Measurement ID	Bed ID	Fault strike (°)	Fault dip (°)	Slickenline rake (°)	Fault displacement (cm)
F1	U3	55	61	90	3
F2	U1	235	45	90	2
F3	U1	232	48	indeterminate	9
F4	U1	223	47	90	1
F5	U1	58	67	92	>2.5
F6	U1	239	65	90	15
F7	U1	46	58	87	12
F8	U1	225	47	90	7
F9	U1	64	58	78	0.5

displacements of ~1 cm and 4 cm, respectively, show evidence for terminations within an apparently weak, clay-rich interval (Fig. 5c). These faults are interpreted as being kinematically related, though they do not appear to be hard-linked across this 5 cm thick interval. This suggests that deformation in this interval in Figure 5c may have been accommodated by ductile strain rather than brittle deformation.

The fault zone described above also extends below Units 8 and 9 into the underlying Unit 10 and Unit 11 packstones (Fig. 5a). Fault surfaces with displacements of less than 1 cm are relatively abundant in Units 10 and 11, and slickenlines on these faults show evidence for approximately dip-slip displacement (Fig. 5e, f). These small-scale faults trend approximately ENE–WSW (parallel to the Hidden Valley fault) but dip to both the NNW and SSE. In some cases, conjugate normal faults in Units 10 and 11 form small graben structures (Fig. 5e).

4.c. Digital fracture mapping

The initial phase of digital fracture mapping focused on bedding pavements P8, P7, P6 and P5 (Fig. 6), which represent the top bedding surfaces of Units 1, 5, 8 and 9–10, respectively (Fig. 2a). Digitally mapped fractures were visually compared to the published field-mapping-derived fracture maps of McGinnis *et al.* (2015) for pavements 5–8 and our results were generally in agreement with no major discrepancies (compare Fig. 6a with fig. 1 in McGinnis *et al.* 2015). Combined fault and fracture intensity (total fracture length per unit area (m/m^2)) was calculated for each of the digitally mapped pavements (Fig. 6b), and average values were found to be in general agreement with the results of McGinnis *et al.* (2015). This initial step was undertaken to validate digital fracture maps generated by interpreting fractures on a georectified orthomosaic. These digitized fracture traces were not projected onto a 2D cross-section in subsequent analysis steps, as was carried out for fractures identified in vertical exposure surfaces.

The second phase of digital fracture mapping focused on vertical bed exposures, and fault and fracture penetration across lithologic units (see Fig. 2b for faults and fractures mapped in 3D). Digital fault and fracture mapping focused on (i) faults identified in the field (Figs 2, 4) that were also visible on the photogrammetric reconstruction (Fig. 5), and (ii) faults and fractures identified in the photogrammetric reconstruction with trends approximately parallel to both the Hidden Valley fault and our field measurements of fault orientations. Orientations of digitally identified faults and fractures were measured on the photogrammetric point-cloud in

CloudCompare, using the Compass 2.0 tool (Thiele *et al.* 2017). Field and digital orientation measurements show relatively close agreement for lower-angle fractures and faults in Units 1 and 3 (Fig. 7a, b). Average strike and dip values for field and digital data are 056°/61° (field data) and 057°/57° (digital data) for faults and fractures synthetic to the Hidden Valley fault, and 240°/49° (field data) and 231°/50° (digital data) for antithetic faults and fractures. Average strike and dip measurements for synthetic faults and fractures show close agreement with the orientation of the Hidden Valley fault (strike/dip of 057°/67°; Ferrill *et al.* 2011). Both field and digital orientations of synthetic faults and fractures exhibit lower variability in measured orientations, with angular standard deviations of 6.7° for field data and 6.1° to 14.7° for digital data. Measured orientations of faults and fractures antithetic to the Hidden Valley fault exhibit higher variability than synthetic faults, with angular standard deviations of 8.7° for field data and 10.5° to 14.7° for digital data. High-angle fractures antithetic to the Hidden Valley fault show the greatest variability of sample populations (Fig. 7c), with an angular standard deviation of 14.7°, but the average strike of these high-angle fractures (ENE 060°–WSW 240°) is approximately parallel to the Hidden Valley fault. Fault and fracture orientations, calculated measurement averages and angular standard deviations for data subsets are provided in online Supplementary Material Table S1.

4.d. Cross-section interpretations

To quantify vertical variations in fracture abundance, fracture containment and vertical persistence of fractures across lithologic boundaries, digitally mapped faults and fractures with trends approximately parallel to the Hidden Valley fault (Fig. 7c) were projected onto a 147°–327° oriented vertical cross-section (Fig. 8a). Bed boundaries interpreted in 3D, as well as an interpretation boundary defined during fieldwork, were also projected onto the cross-section, allowing us to quantify 2D cross-section areas of each exposed lithologic unit at the study site. Projected fault and fracture polylines in cross-section view highlight the overall tendency for more high-angle fractures (dashed lines in Fig. 8a) to terminate at bed interfaces. Lower-angle fractures (thin solid lines) and faults (thick solid lines) are more likely to cross bed boundaries and multiple lithologic units. Lower-angle fractures appear to be more abundant where identified faults are present, and with the exception of fractures in Unit 5, both faults and fractures through the exposed section exhibit a wide range of apparent spacings. Fracture patterns exhibit variability throughout the cross-section,
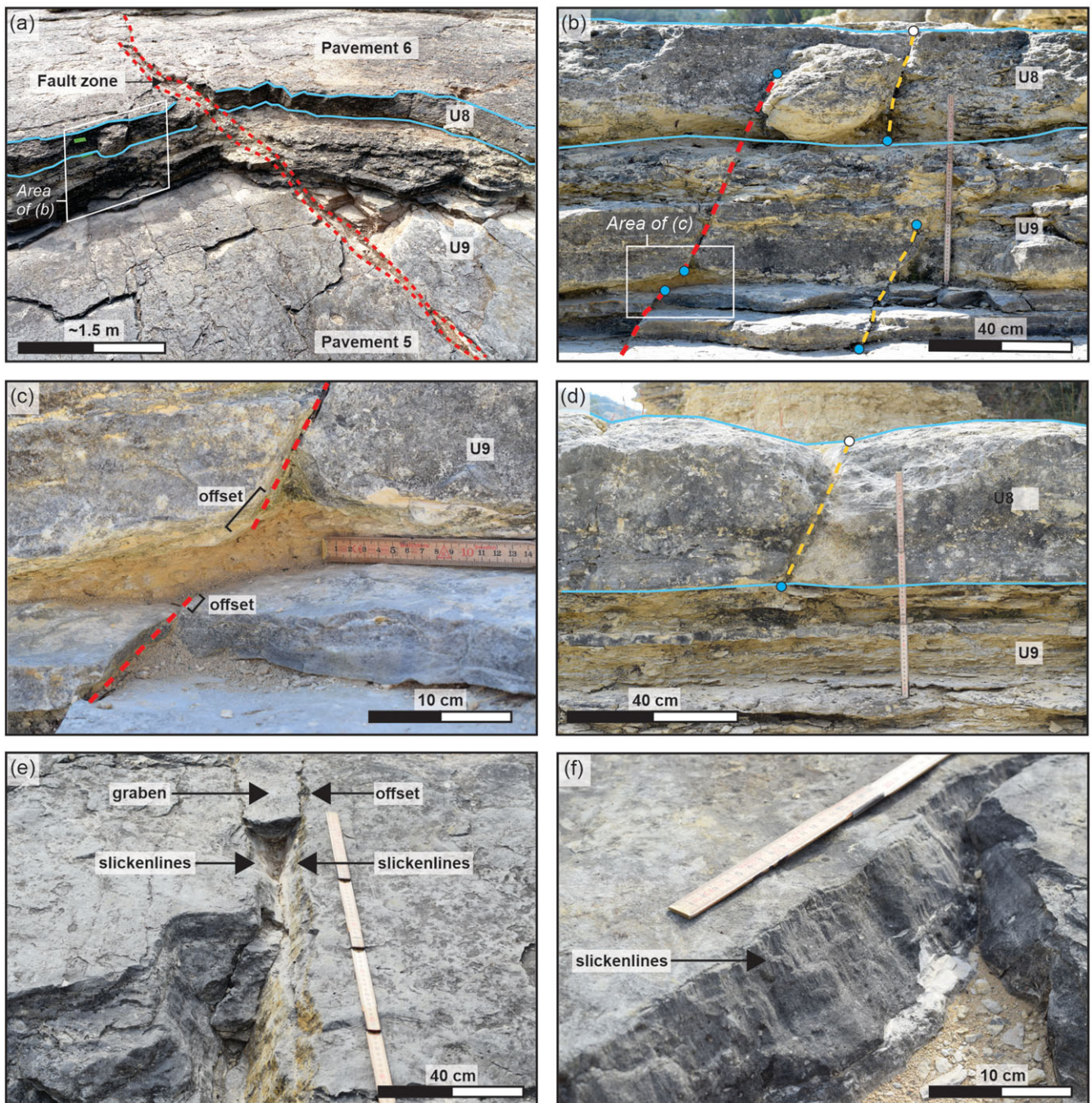
Fig. 5. Field examples of faults and fractures in the study site. (a) Fault zone crossing multiple mechanical boundaries and lithologic units. (b) A fault with visible displacement and two sub-parallel, high-angle fractures with no detectable offset. (c) Enlarged view of (b) showing soft-linkage of two normal fault segments across a clay-rich wackestone interval. (d) Example of high-angle, strata-bound fracture that does not cross the upper or lower interface boundaries of Unit 8. (e) Conjugate normal faults (with visible offset and slickenlines along fault surfaces) and associated graben structure in Unit 10. (f) Fault with exposed slickenlines in Unit 10. See Figure 2a for field photograph locations. Key for fault and fracture colour scheme shown in Figure 4. Blue lines in parts (a), (b) and (d) denote lithologic unit boundaries.

and in general, faults and fractures are largely strata-bound or confined to units of similar composition (Fig. 8a).

4.d.1. Units 1–3

Fault and fracture patterns are relatively consistent through Units 1–3 (Fig. 8a), with brittle failure surfaces dominantly represented by conjugate normal faults and lower-angle fractures. The Unit 2 wackestone, which has a measured thickness of 0–5 cm and a relatively high weight percentage of clay (6.6 %), marks the intermediate boundary between Units 1 and 3. Although several fractures abut against Unit 2 (Fig. 4b), this thin interval did not consistently arrest faults and lower-angle fractures (Fig. 8a), despite relatively high clay content. We interpret that Units 1 and 3 generally acted as a single mechanical stratigraphic unit with respect to fracture initiation and propagation.
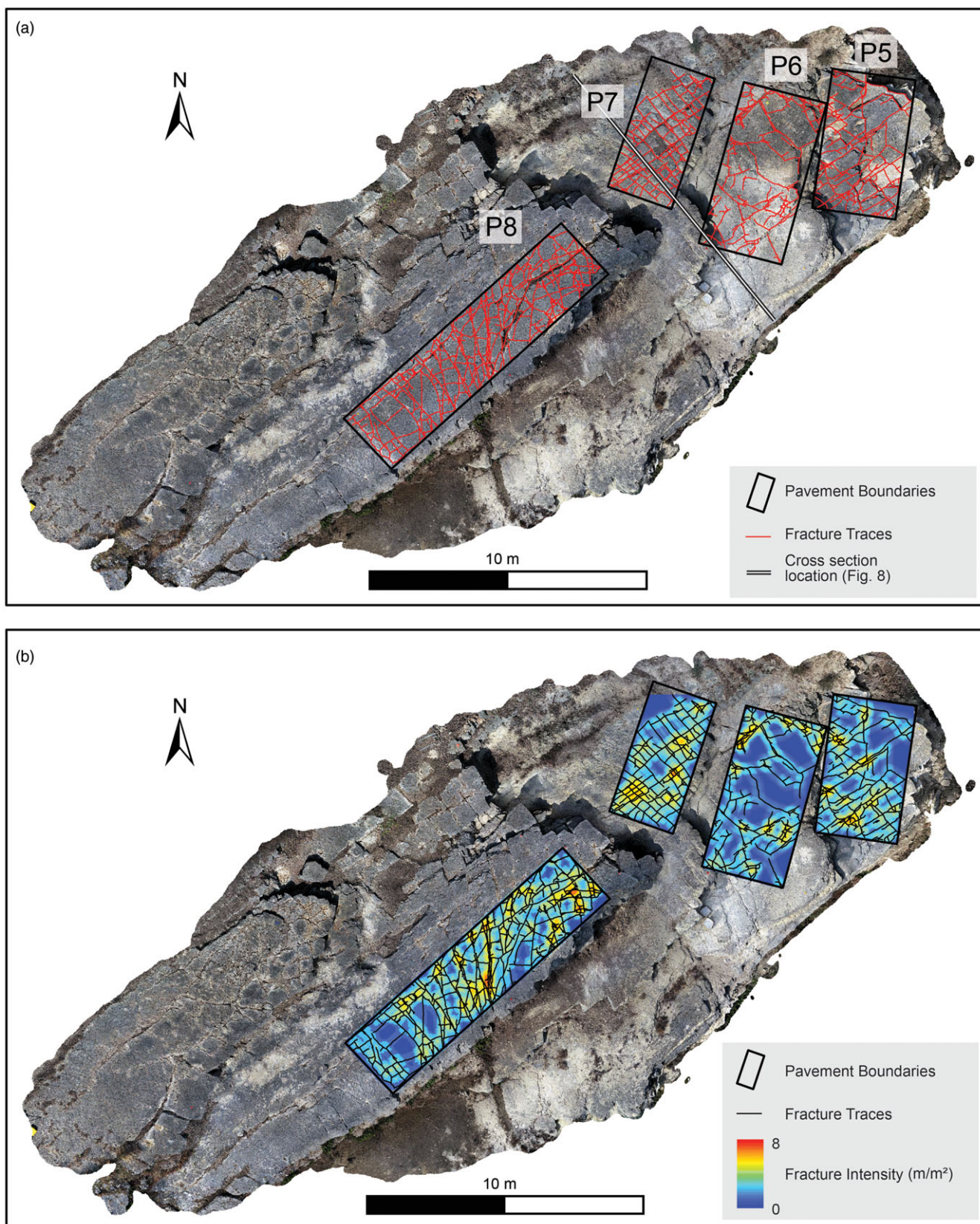
Fig. 6. (a) High-resolution orthomosaic with pavement outlines (black) with fault and fracture traces (red, undifferentiated) digitized from the high-resolution orthomosaic. See McGinnis *et al.* (2015) for a comparison of field-mapping-derived fault and fracture traces. (b) Orthomosaic with outlines of pavements 5, 6, 7 and 8, fault and fracture traces (undifferentiated) and calculated areal fault and fracture intensities (fracture length per unit area). Fault and fracture intensities calculated using the Line Density tool in ArcMap 10.5.1 (ESRI) with an output cell size of 0.05 m and a search radius of 0.5 m. See Figure 1 for location.
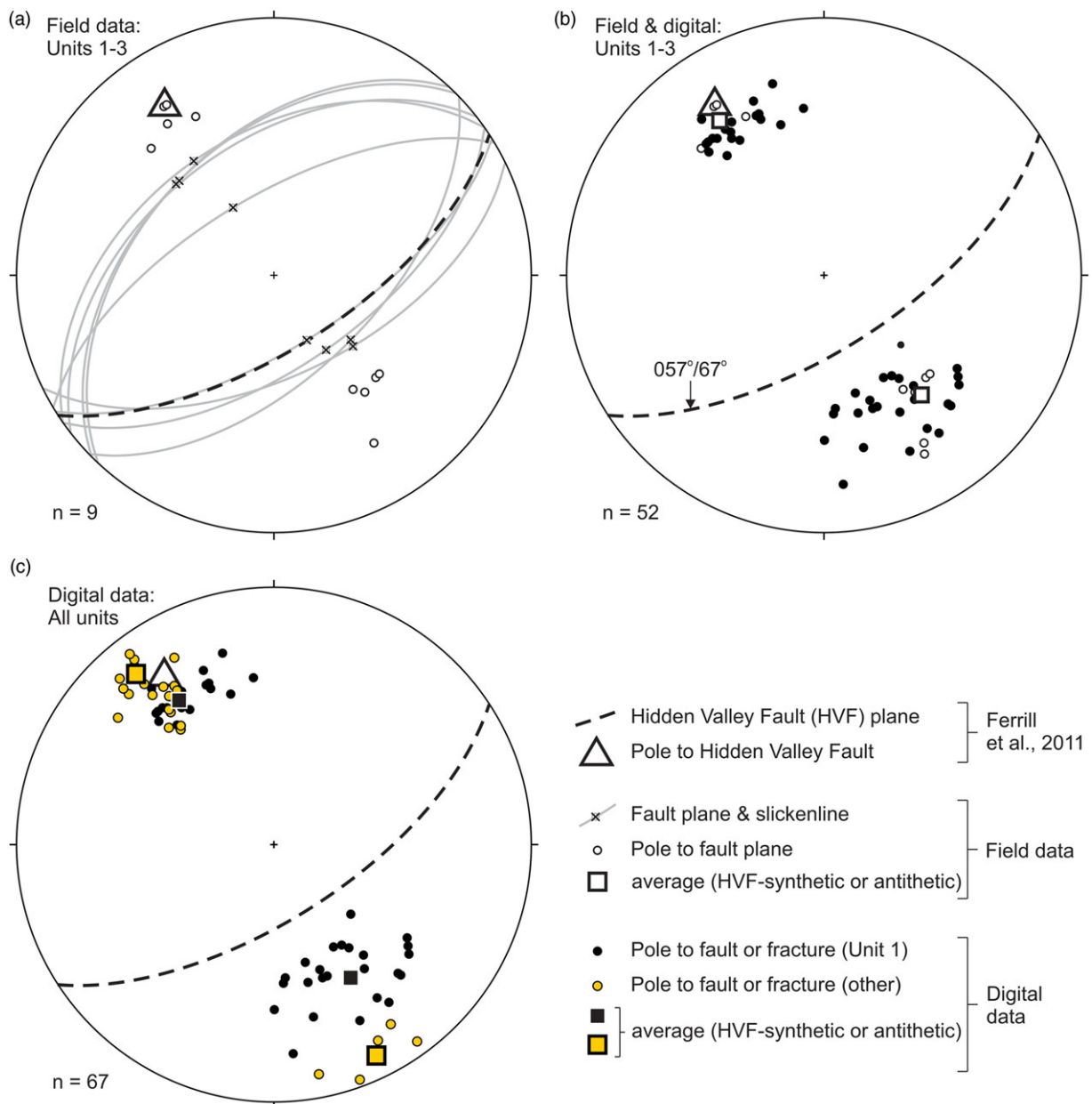
Fig. 7. Orientation data for faults and fractures with trends parallel or sub-parallel to the Hidden Valley Fault, which is shown by thick dashed lines (fault plane) and square symbols (pole to fault plane). (a) Great circles, poles and slickenline orientations for faults observed and measured in the field. (b) Poles to field-measured faults and digitally mapped faults and lower-angle (<70°) fractures striking parallel or sub-parallel to the Hidden Valley Fault. (c) Poles to faults, high-angle fractures and lower-angle fractures identified and mapped on the digital outcrop, with orientations extracted from the photogrammetric point-cloud. All projections on equal-area lower hemisphere stereonets.

4.d.2. Unit 4

Although no observed faults or fractures cross the entire wacke-stone interval of Unit 4, several faults and lower-angle fractures in Units 1–3 do not terminate at the U3–U4 boundary but appear to have propagated as much as 15 cm downwards into the upper part of the Unit 4 wackestone (Figs 4d, 8a, 6d). The Unit 4 wacke-stone is represented by relatively high clay content (9.6 %) and low average rebound (12.9) values (Table 1).

4.d.3. Unit 5

Deformation features in Unit 5 packstone (immediately below Unit 4) are dominated by high-angle fractures (Fig. 8a). With

the exception of one observed failure surface, these fractures are generally bed-contained and do not show evidence for upward propagation into the lower part of Unit 4. In addition, the high-angle fractures in Unit 5 are relatively evenly spaced, in contrast to all other beds in the exposure where fractures are not regularly spaced.

4.d.4. Unit 6

With the exception of a single high-angle fracture that crosses Units 5 and 6 (Fig. 8a), packstone-dominated Unit 6 is nearly devoid of faults and fractures. Unlike Units 1 and 3, which appear to be relatively homogeneous packstones, Unit 6 is characterized by centimetre-scale alternations between thin wackestone and packstone beds.
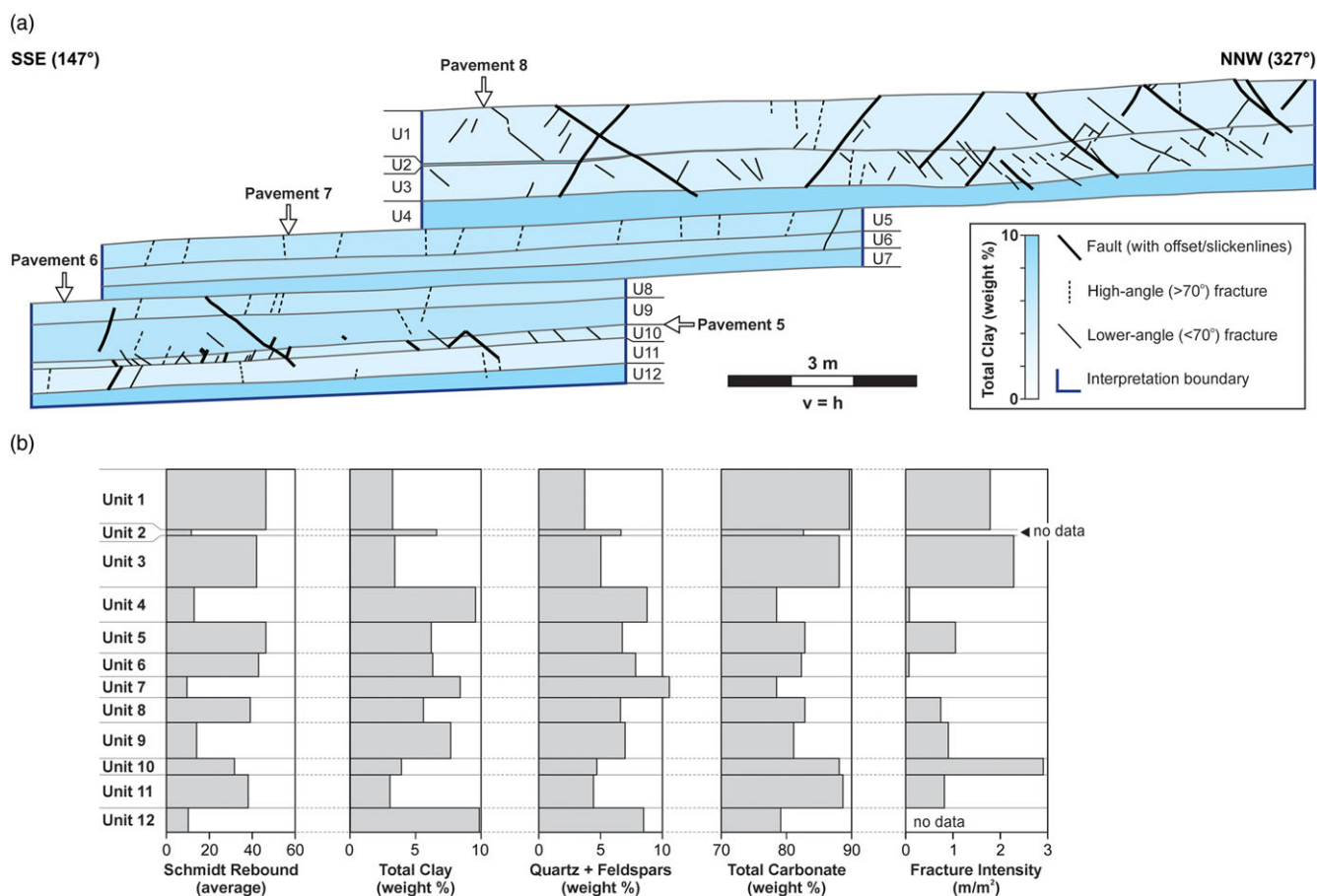
Fig. 8. (a) SSE–NNW cross-section showing projected polyline interpretations of bedding horizons, faults and fractures. Lithologic units coloured according to clay content (see key) and faults and fractures coloured according to classification scheme; see main text for details. (b) Mean Schmidt rebound, weight per cent total clay, weight per cent quartz and feldspar, weight per cent total carbonate and calculated fracture intensities for each lithologic unit.

4.d.5. Unit 7

No faults or fractures are observed in Unit 7. This interval is somewhat analogous to Unit 4 in that it is a wackestone interval with low measured rebound, relatively high clay content and few or no faults and fractures.

4.d.6. Units 8–11

Fault and fracture terminations through Units 8–11 are apparently less systematic than in the intervals above (Fig. 8a), with structures through this interval showing little evidence for containment at a specific horizon or stratigraphic level. All of the mapped bed boundaries in the Unit 8 to Unit 12 section are crossed by both faults and fractures. Higher fault and fracture connectivity across these layers is observed in the cross-section (Fig. 8a) despite variations in both composition and measured rebound (Fig. 8b). Strata-bound faults and fractures are contained within these intervals (e.g. several lower-angle fractures in Unit 10), but the general pattern is one of greater variability in patterns of fracture containment.

4.d.7. Clay content versus fracture patterns in cross-section

Measured weight per cent of clay for each of the 12 lithologic units (Table 1) was used for shading lithology polygons in the cross-section, allowing for a visual appraisal of clay content versus fault and fracture characteristics through the exposed section (Fig. 8a). Based on clay content variations through the

exposed section (Table 1), there appears to be a link between the abundance of clay in each lithologic unit and fault and fracture occurrence (Fig. 8a). Units 1, 3, 10 and 11 have the lowest clay percentages (<4 %) of the lithologic units (Figs 8b, 9), and relatively high numbers of faults and fractures are present in these units.

4.e. Calculated fracture intensity versus measured rock properties

Fracture intensity (m/m^2) for Units 1–12 was calculated by dividing the total length of combined fault and fracture traces within a given unit in cross-section by the area of that unit within the interpretation boundary (see Fig. 8a for interpretation boundary). This calculation provides an average fracture intensity for each unit (Table 1; Fig. 8b) and allows average fracture intensity to be compared to composition, Schmidt rebound and thickness of each lithologic unit.

We find an inverse relationship between fracture intensity and total clay content (weight %), with a moderate correlation coefficient for this relationship of 0.49 (Fig. 9a). Combined quartz and total feldspars (potassium and plagioclase) content also correlates with fracture intensity ($R^2 = 0.79$), with data showing increased fracture intensities with lower weight percentages of these detrital components (Fig. 9b). Carbonate content in this case
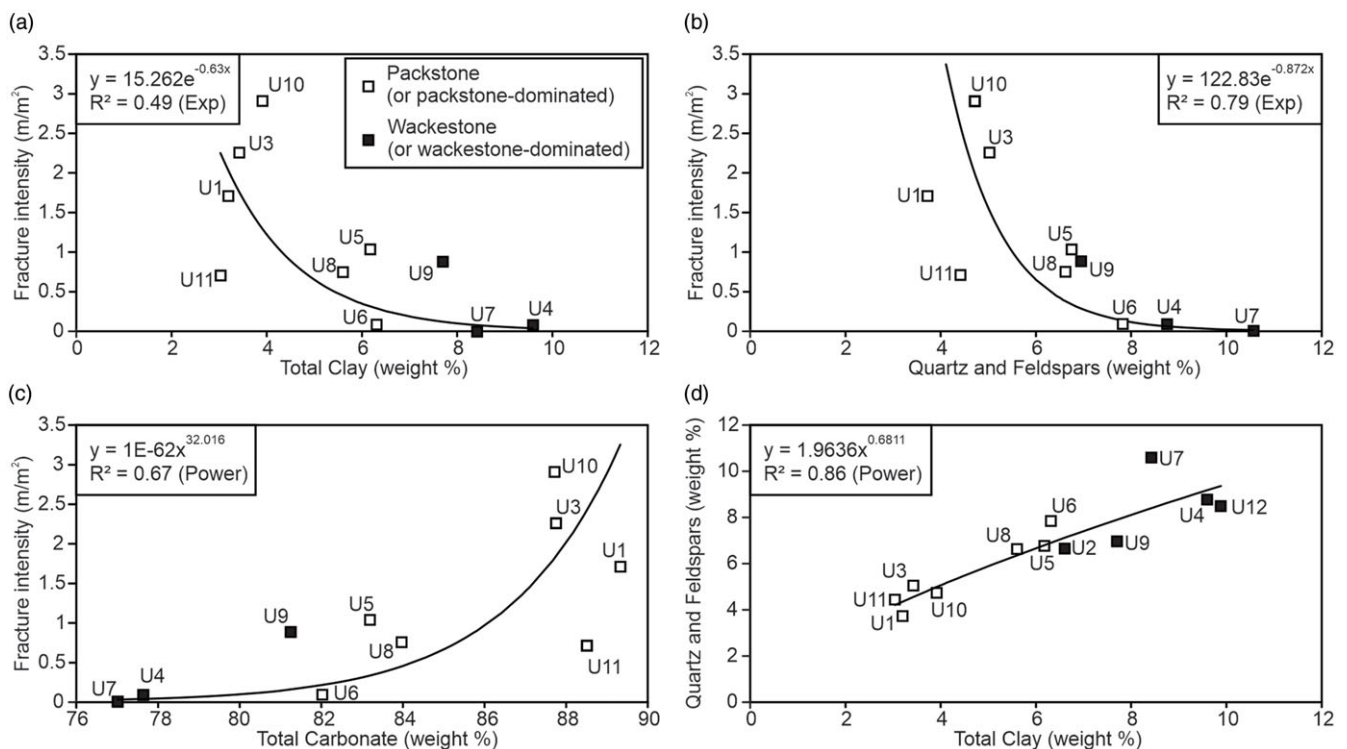
Fig. 9. (a–c) Cross-plots of calculated fracture intensity (from cross-section) versus unit composition data. (d) Summed quartz and feldspar content versus weight per cent total clay for all units. Unit numbers (see Fig. 2) shown on each cross-plot.

approximately represents the balance of mineral content (along with total clay, quartz and feldspars), and yields a relatively strong correlation ($R^2 = 0.67$) and a trend representing increased fracture intensity with increased carbonate mineral content (Fig. 9c). Total carbonate within this sample suite represents the summed weight percentage of calcite, dolomite and siderite for each sample. Except for Unit 9 (which contains 2.4 % dolomite), all samples contain less than 0.6 % combined dolomite and siderite, with the remaining total carbonate in each sample made up of calcite (online Supplementary Material Table S2). Total clay content in samples correlates well ($R^2 = 0.86$) with summed quartz and feldspars (Fig. 9d), which may be indicative of either authigenic (feldspar-derived) or detrital clay content.

Combined fault and fracture intensity correlates moderately with average Schmidt rebound values ($R^2 = 0.46$; Fig. 10a). Average Schmidt rebound shows a moderate positive correlation with total carbonate ($R^2 = 0.62$; Fig. 10b) and a moderate negative correlation with total clay ($R^2 = 0.65$; Fig. 10c). Finally, of all assessed variables, average bed thickness exhibits the weakest apparent relationship to fracture intensity, with a correlation coefficient of 0.16 (Fig. 10d).

5. Discussion

5.a. Fault and fracture categorization

Extensional faults identified in the study area are either synthetic (SE-dipping) or antithetic (NW-dipping) to the Hidden Valley fault (Fig. 7a). Conjugate (synthetic and antithetic) normal faults are relatively common in the footwall to the Hidden Valley fault at Canyon Lake Gorge (Ferrill & Morris, 2008; Ferrill *et al.* 2009), and

these have been interpreted as early formed structures related to monocline development (e.g. Ferrill *et al.* 2009, 2011). We therefore interpret the faults identified in the study area as consistent with early formed, monocline-related faults that formed in a normal-faulting regime at Canyon Lake Gorge, as documented by Ferrill *et al.* (2011). Lower-angle fractures identified in digital data with trends sub-parallel to the Hidden Valley fault are generally oriented sub-parallel to synthetic and antithetic extensional faults identified in the field (Fig. 7a, b). The similarity between orientations of lower-angle fractures and conjugate normal faults suggests that these structures may be genetically related, and therefore that both the observed faults and lower-angle fractures formed as a result of shear failure even though clear evidence for slip is not present on the lower-angle fractures. Shear behaviour for the lower-angle fractures is compatible with the normal-faulting stress regime (i.e. vertical maximum principal stress), and NNW–SSE-oriented minimum principal stress direction that has been interpreted for the Hidden Valley fault system and Balcones fault system (e.g. Ferrill *et al.* 2004, 2011, 2012a, 2020a; Ferrill & Morris, 2008; Morris *et al.* 2016).

While it is theoretically possible that the observed lower-angle fractures formed through tensile failure, this interpretation would require a *c.* 90° rotation in minimum principal stress direction to produce the oppositely dipping lower-angle fractures (Fig. 8a). Specifically, if both NNW- and SSE-dipping lower-angle fractures formed by tensile failure perpendicular to the minimum principal stress direction, the minimum principal stress would have been inclined 40–50° from horizontal – plunging SSE during formation of NNW-dipping fractures, and plunging NNW during formation of SSE-dipping fractures – a scenario that we envision as unlikely. Our preferred interpretation, therefore, is that lower-angle
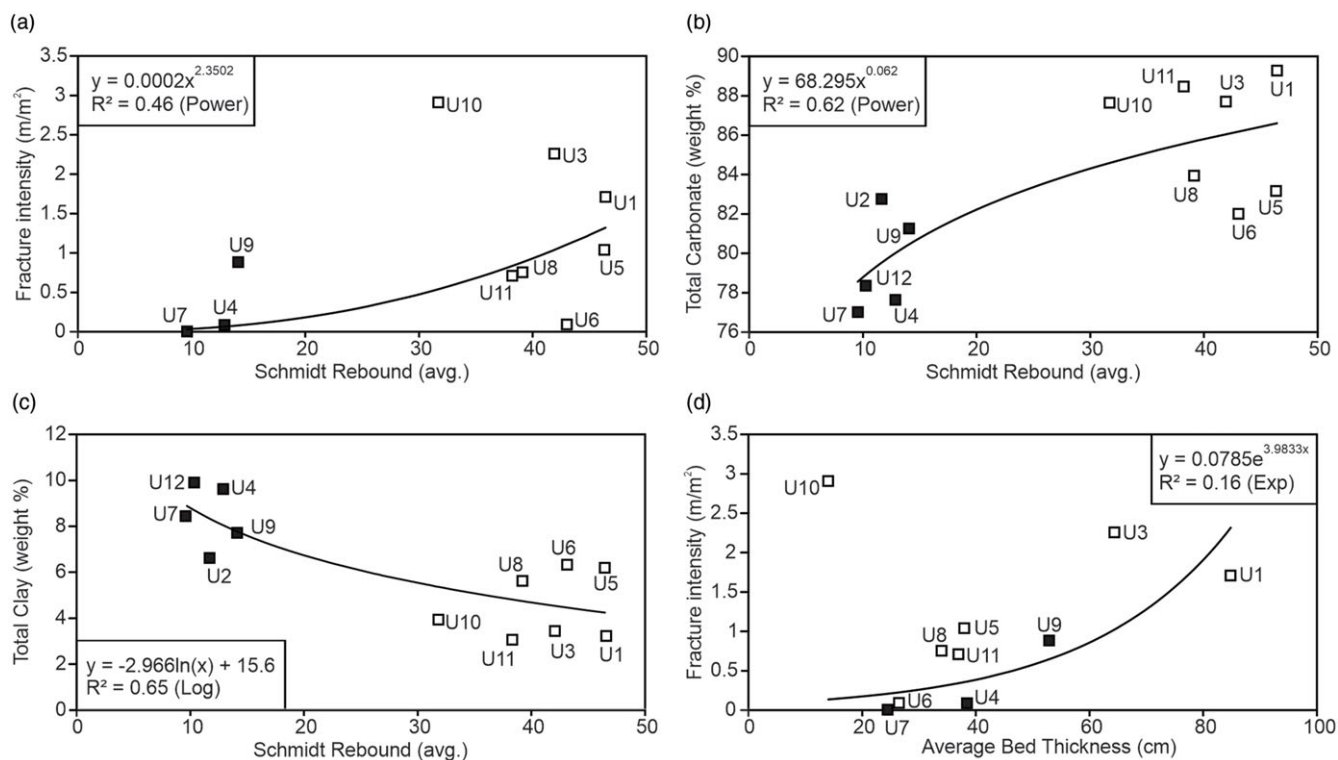
Fig. 10. (a) Fault and fracture intensity versus Schmidt rebound. (b) Total carbonate versus Schmidt rebound. (c) Total clay versus Schmidt rebound. (d) Fault and fracture intensity versus average bed thickness. See Figure 9 for symbol key.

fractures observed at the site are incipient shear failure surfaces that did not accumulate sufficient slip to offset bedding planes by a detectable amount, or to form observable slickenlines. We acknowledge that the lack of mineralization and associated mineral textures on lower-angle fracture surfaces rules out definitive categorization of failure mode for these structures. The consistency of their orientations with both observed normal faults at the site and the Hidden Valley fault, however, provides a reasonable basis for interpreting these structures as incipient shear fractures.

We interpret high-angle fractures with trends sub-parallel to the Hidden Valley fault (Fig. 7c) as having formed as a result of tensile failure in a normal-faulting stress regime. This interpretation requires a maximum principal stress orientation close to vertical and a subhorizontal NNW–SSE-oriented minimum principal stress direction. This is consistent with (i) the orientation of the Hidden Valley fault (Ferrill & Morris, 2008; Ferrill *et al.* 2011), (ii) normal fault orientations in the study area (Fig. 7a), and (iii) our interpretation of lower-angle fractures at the site as incipient shear fractures. There also appears to be a general pattern in cross-section view (Fig. 8a) for high-angle fractures to consistently terminate at bed boundaries, whereas both normal faults and low-angle fractures more commonly cross mechanical boundaries. This general pattern may further support our interpretation of lower-angle fractures as incipient shear fractures and high-angle fractures as tensile failure surfaces, given that opening-mode fractures are more likely than shear fractures to terminate at weak mechanical boundaries as well as at pre-existing faults and unfilled fractures (c.f. Cooke *et al.* 2006; Ferrill *et al.* 2014). Previous work has shown that the fracture network in the Hidden Valley fault zone at Canyon Lake Gorge is in many cases dominated by shear fractures (small faults; Ferrill *et al.* 2011; McGinnis *et al.* 2015).

McGinnis *et al.* (2015) interpreted that major fracture system development initiated near maximum burial at relatively high differential stress where shear failure dominated over tensile failure, and that subsequent tensile failure likely occurred under lower differential stress conditions and filled in between shear fractures.

5.b. Unit composition versus fracture intensity

The composition of lithologic units appears to be a dominant control on fracture occurrence at the study area. Moderate to high fault and fracture intensities occur where total clay is relatively low and carbonate mineral percentages are relatively high (Fig. 9a–c). Note the strong correlation between total clays and quartz–feldspar components (Fig. 9d), which we attribute to either input of detrital clay, quartz and feldspars in a carbonate depositional setting, or authigenic transformation of silicate minerals (feldspars) to clay during progressive burial diagenesis. The genetic relationship between quartz, feldspars and total clays is beyond the scope of this study but we note that quartz and feldspar weight percentages are inversely correlated with rock strength in the carbonate succession here, while a positive correlation between quartz content and rock strength is generally expected in clastic sedimentary and crystalline rocks (e.g. Chang *et al.* 2006 and references therein).

Correlations from our data indicate (i) a general increase in fracture intensity with increasing rebound (Fig. 10a), (ii) an increase in measured rebound with increasing carbonate content (Fig. 10b), and (iii) a decrease in average rebound with increasing clay content (Fig. 10c). The general relationships of increasing fracture intensity with increasing rebound, decreasing clay content and increasing carbonate content suggest that faults and fractures are more likely to occur in cleaner (i.e. clay-poor, carbonate-rich),

more competent units. This observation is consistent with previous outcrop studies and experimental work (e.g. Donath, 1970; Wu & Pollard, 1991; Hovorka, 1998; Laubach *et al.* 2009; Roche *et al.* 2012; Roche & van der Baan, 2013; Ferrill *et al.* 2014, 2017b; Cawood & Bond, 2018), which document that more competent lithologies accommodate lower amounts of strain before the onset of brittle failure (i.e. have lower ductility; Donath, 1970). Our measured rebound versus clay content, rebound versus fault and fracture intensity, and clay content versus fault and facture intensity results suggest that more clay-rich wackestone intervals in the study area likely accommodated extensional strain associated with regional Gulf of Mexico extension (Ferrill *et al.* 2017a) through ductile deformation. Previous work from Canyon Lake Gorge, and elsewhere in the region (e.g. Ferrill *et al.* 2012b), shows that clay-rich layers are more likely to experience thickness changes due to ductile deformation. In contrast, more competent packstone units experienced brittle deformation by shear or hybrid failure in faults and fractures synthetic and antithetic to the Hidden Valley fault, and by tensile failure for opening-mode, high-angle fractures.

We acknowledge the presence of small-scale (<5 cm) faults and fractures in finely bedded intervals (e.g. Units 6 and 9; Fig. 2) that were not practicable to identify and map comprehensively. These small-scale structures, where observed, are contained in thin (<5 cm) weathering-resistant intervals and were not mapped unless they persist across interbeds (e.g. Fig. 4d). As these <5 cm structures do not connect vertically across interbeds, we interpret their potential effect on large-scale permeability architecture as negligible.

5.c. Unit interfaces

Abrupt changes in unit composition, fault and fracture intensity, and brittle failure mode through the succession provide evidence for the influence of lithology on deformation style. Unit interfaces, however, appear to play less of a role in our study area than has been documented in other outcrop studies (e.g. Gillespie *et al.* 1999; Hooker *et al.* 2013; McGinnis *et al.* 2017) and in results from numerical modelling (e.g. Cooke & Underwood, 2001; Chang *et al.* 2015). These studies show that the shear strength of layer boundaries is an important factor, and that bed-perpendicular opening-mode fractures tend to terminate at weak interfaces whereas fractures can grow across strong interfaces. This may explain the systematic terminations of high-angle fractures at the upper and lower boundaries of Unit 5 and, to a lesser degree, at the upper and lower boundaries of Unit 8 (Fig. 8a).

It should be noted that each of the four boundaries referred to above represent a transition from more highly fractured, more competent layers to less competent layers with low fracture intensity (Fig. 8b). Differentiating between interface strength versus unit strength as a control on containment of opening-mode fractures is therefore not tractable in these cases. For the most part, normal faults and lower-angle fractures cross multiple units entirely with no apparent change in fracture orientation (e.g. at U1–U2–U3 transition; Fig. 8a) and only rarely terminate directly at unit interfaces (Fig. 8b). At interfaces between units of contrasting clay content and rebound values (e.g. U3–U4 and U9–U10 boundaries; Fig. 8a) shear fractures typically cross interfaces and terminate within less competent units. It should be noted that interfaces with low shear strength do not inhibit the growth of shear fractures or faults as has been interpreted to occur in the case of opening-mode fractures (Cooke *et al.* 2006; Ferrill *et al.* 2014).

5.d. Unit thickness versus fracture intensity

As documented by McGinnis *et al.* (2015), there is little correlation between bed thickness and fracture intensity in the study area. We find that bed thickness versus fracture intensity is poorly correlated ($R^2 = 0.16$) compared with the other explored variables, and surprisingly our data suggest, if anything, that increased bed thickness correlates with higher fracture intensity (Fig. 10d). This result is unexpected (in spite of the poor correlation and U10 outlier; Fig. 10d) as many examples in the existing literature have documented an inverse relationship between bed thickness and fracture abundance, with thinner beds exhibiting higher fracture intensities, increased fracture frequencies or lower fracture spacings (e.g. Harris *et al.* 1960; Price, 1966; McQuillan, 1973; Ladeira & Price, 1981; Corbett *et al.* 1987; Huang & Angelier, 1989; Narr & Suppe, 1991; Bai & Pollard, 2000; Nelson, 2001; Yin, 2010; McGinnis *et al.* 2017). Most studies, however, focus on (i) more competent beds, where fractures are typically better developed (see McGinnis *et al.* 2015 and references therein), and (ii) fracture abundance versus unit thickness relationships in beds or units that are compositionally similar (e.g. Narr & Suppe, 1991). The role of composition, particularly in less competent, clay-rich rocks is, therefore, commonly overlooked in the generally accepted paradigm of bed thickness to fracture abundance (spacing, frequency, intensity) ratios.

As noted by Olson (2004), unit thickness is only one of several parameters that may govern fracture spacing in sedimentary rocks, with others including those listed above. Our lithologic units exhibit a relatively wide range of compositions and rebound values, and we show that composition exerts a dominant control on mechanical rebound, style of deformation, fracture intensity and fracture containment through this sequence of mechanically layered carbonates. Given the dominance of composition in defining deformation mode and fracture containment, it is perhaps not surprising that we do not find a robust relationship between bed thickness and fracture intensity. Despite these observations, we find that unit thicknesses do play a role in fracture containment and propagation. Shear failure surfaces appear to have propagated across relatively thin clay-rich layers (e.g. Unit 2) but not across clay-rich, weak layers with thicknesses greater than 5–10 cm (e.g. Unit 4). The ability for a shear failure surface to propagate across weak layers in multilayer successions likely depends on (i) fault displacement magnitude, (ii) ductility contrasts through deformed successions, and (iii) relative thicknesses of competent and incompetent layers. Future work quantifying relationships between these factors will likely elucidate fault growth processes, patterns of fault displacement and the potential ability for brittle failure surfaces to connect rock volumes across strata.

6. Conclusions

We present a detailed field-based and digital analysis of fracture characteristics (orientation, failure mode, vertical persistence, intensity) and lithologic properties (texture, composition, rebound, bed thickness) in a Cretaceous carbonate packstone and wackestone succession at Canyon Lake Gorge, Texas. We find that mechanical stratigraphy plays an important role in fault and fracture propagation and containment.

(1) Unit composition, specifically clay minerals versus carbonate content, controls deformation style, fracture intensity and fracture containment. Relatively clay-rich wackestone

lithologies exhibit low fracture intensities, and both opening-mode fractures and faults within competent packstone units systematically terminate at competent–incompetent unit interfaces, or within relatively weak, clay-rich units.

(2) Our data show poor correlations between layer thickness and fracture intensity. We attribute this to the relatively wide range of compositions in lithologic units and the dominant role of lithology and composition in defining fracture occurrence and containment at the site.

(3) While no clear relationships between layer thickness and fracture abundance are recorded at the site, we find that thicknesses of relatively incompetent, clay-rich layers control the likelihood for faults and fractures to propagate across layer boundaries. This result is important for potential vertical connectivity of faults and fractures in mechanically layered carbonates containing variable proportions of relatively strong and weak layers.

References

Agar SM and Geiger S (2015) Fundamental controls on fluid flow in carbonates: current workflows to emerging technologies. In *Fundamental Controls on Fluid Flow in Carbonates: Current Workflows to Emerging Technologies* (eds SM Agar and S Geiger), pp. 1–59. Geological Society of London, Special Publication no. 406.

Atkinson BK (1984) Subcritical crack growth in geological materials. *Journal of Geophysical Research* **89**, 4077–114.

Aydin A and Basu A (2005) The Schmidt hammer in rock material characterization. *Engineering Geology* **81**, 1–14.

Bai T and Pollard D (2000) Fracture spacing in layered rocks: a new explanation based on the stress transition. *Journal of Structural Geology* **22**, 43–57.

Bauer H, Schröckenfuchs TC and Decker K (2016) Hydrogeological properties of fault zones in a karstified carbonate aquifer (Northern Calcareous Alps, Austria). *Hydrogeology Journal* **24**, 1147–70.

Bisdom K, Bertotti G and Bezerra FH (2017) Inter-well scale natural fracture geometry and permeability variations in low-deformation carbonate rocks. *Journal of Structural Geology* **97**, 23–36.

Bodziak R, Clemons K, Stephens A and Meek R (2014) The role of seismic attributes in understanding the hydraulically fracturable limits and reservoir performance in shale reservoirs: an example from the Eagle Ford Shale, south Texas. *American Association of Petroleum Geologists Bulletin* **98**, 2217–35.

Bourne SJ (2003) Contrast of elastic properties between rock layers as a mechanism for the initiation and orientation of tensile failure under uniform remote compression. *Journal of Geophysical Research: Solid Earth* **108**, 1–12.

Brenner SL and Gudmundsson A (2004) Arrest and aperture variation of hydrofractures in layered reservoirs. In *The Initiation, Propagation, and Arrests of Joints and Other Fractures* (eds JW Cosgrove and T Engelder), pp. 117–28. Geological Society of London, Special Publication no. 23.

Cawood AJ and Bond CE (2018) 3D mechanical stratigraphy of a deformed multi-layer: linking sedimentary architecture and strain partitioning. *Journal of Structural Geology* **106**, 54–69.

Cawood AJ, Bond CE, Howell JA, Butler RWHB and Totake Y (2017) LiDAR, UAV or compass-clinometer? Accuracy, coverage and the effects on structural models. *Journal of Structural Geology* **98**, 67–82.

Cawood AJ, Corradetti A, Granado P and Tavani S (2022) Detailed structural analysis of digital outcrops: a learning example from the Kermanshah-Qulqula radiolarite basin, Zagros basin, Iran. *Journal of Structural Geology* **154**, 104489.

Chang X, Shan Y, Zhang Z, Tang C and Ru Z (2015) Behavior of propagating fracture at bedding interface in layered rocks. *Engineering Geology* **197**, 33–41.

Chang C, Zoback MD and Khaksar A (2006) Empirical relations between rock strength and physical properties in sedimentary rocks. *Journal of Petroleum Science and Engineering* **51**, 223–37.

Cilona A, Aydin A, Likerman J, Parker B and Cherry J (2016) Structural and statistical characterization of joints and multi-scale faults in an alternating sandstone and shale turbidite sequence at the Santa Susana Field Laboratory: implications for their effects on groundwater flow and contaminant transport. *Journal of Structural Geology* **85**, 95–114.

Clarke BA and Burbank DW (2011) Quantifying bedrock-fracture patterns within the shallow subsurface: implications for rock mass strength, bedrock landslides, and erodibility. *Journal of Geophysical Research: Earth Surface* **116**, 1–22.

Cooke ML, Simo JA, Underwood CA and Rijken P (2006) Mechanical stratigraphic controls on fracture patterns within carbonates and implications for groundwater flow. *Sedimentary Geology* **184**, 225–39.

Cooke ML and Underwood CA (2001) Fracture termination and step-over at bedding interfaces due to frictional slip and interface opening. *Journal of Structural Geology* **23**, 223–38.

Cooper MA (1991) The analysis of fracture systems in subsurface thrust structures from the foothills of the Canadian Rockies. In *Thrust Tectonics* (ed. KR McClay), pp. 391–405. New York: Springer Science & Business Media.

Corbett K, Friedman M and Spang J (1987) Fracture development and mechanical stratigraphy of Austin Chalk, Texas. *American Association of Petroleum Geologists Bulletin* **71**, 17–28.

De Marsily G, Delay F, Gonçalvès J, Renard P, Teles V and Violette S (2005) Dealing with spatial heterogeneity. *Hydrogeology Journal* **13**, 161–83.

Donath FA (1970) Some information squeezed out of rock. *American Scientist* **58**, 54–72.

Douma L, Regelink JA, Bertotti G, Boersma QD and Barnhoorn A (2019) The mechanical contrast between layers controls fracture containment in layered rocks. *Journal of Structural Geology* **127**, 1–11.

Ferrill DA, Evans MA, McGinnis RN, Morris AP, Smart KJ, Lehrmann D, Gulliver KD and Sickmann Z (2020a) Fault zone processes and fluid history in Austin Chalk, southwest Texas. *American Association of Petroleum Geologists Bulletin* **104**, 245–83.

Ferrill DA, McGinnis RN, Morris AP and Smart KJ (2012a) Hybrid failure: field evidence and influence on fault refraction. *Journal of Structural Geology* **42**, 140–50.

Ferrill DA, McGinnis RN, Morris AP, Smart KJ, Sickmann ZT, Bentz M, Lehrmann D and Evans MA (2014) Control of mechanical stratigraphy on bed-restricted jointing and normal faulting: Eagle Ford Formation, south-central Texas. *American Association of Petroleum Geologists Bulletin* **98**, 2477–506.

Ferrill DA and Morris AP (2003a) Dilational normal faults. *Journal of Structural Geology* **25**, 183–96.

Ferrill DA and Morris AP (2003b) Erratum to: "Dilational normal faults". *Journal of Structural Geology* **25**, 827.

Ferrill DA and Morris AP (2008) Fault zone deformation controlled by carbonate mechanical stratigraphy, Balcones fault system, Texas. *American Association of Petroleum Geologists Bulletin* **92**, 359–80.

Ferrill DA, Morris AP and McGinnis RN (2009) Crossing conjugate normal faults in field exposures and seismic data. *American Association of Petroleum Geologists Bulletin* **93**, 1471–88.

Ferrill DA, Morris AP and McGinnis RN (2012b) Extensional fault-propagation folding in mechanically layered rocks: the case against the frictional drag mechanism. *Tectonophysics* **576–577**, 78–85.

Ferrill DA, Morris AP and McGinnis RN (2019) Geologic structure of the Edwards (Balcones Fault Zone) Aquifer. In *The Edwards Aquifer: The Past, Present, and Future of a Vital Water Resource* (eds JM Sharp Jr, RT Green and GM Schindel), pp. 171–88. Geological Society of America Memoir no. 215.

Ferrill DA, Morris AP, McGinnis RN and Smart KJ (2017a) Myths about normal faulting. In *The Geometry and Growth of Normal Faults* (eds C Childs, RE Holdsworth, CA-L Jackson, T Manzocchi, JJ Walsh and G Yielding), pp. 41–56. Geological Society of London, Special Publication no. 439.

Ferrill DA, Morris AP, McGinnis RN, Smart KJ and Ward WC (2011) Fault zone deformation and displacement partitioning in mechanically layered carbonates: the Hidden Valley fault, central Texas. *American Association of Petroleum Geologists Bulletin* **95**, 1383–97.

Ferrill DA, Morris AP, McGinnis RN, Smart KJ, Wigginton SS and Hill NJ (2017b) Mechanical stratigraphy and normal faulting. *Journal of Structural Geology* **94**, 275–302.

Ferrill DA, Morris AP, Sims DW, Green R, Franklin N and Waiting DJ (2008) Geologic controls on interaction between the Edwards and Trinity Aquifers, Balcones Fault System, Texas. *South Texas Geological Society Bulletin* **48**, 21–45.

Ferrill DA, Sims DW, Waiting DJ, Morris AP, Franklin N and Schultz AL (2004) Structural framework of the Edwards Aquifer recharge zone in south-central Texas. *Geological Society of America Bulletin* **116**, 407–18.

Ferrill DA, Smart KJ and Morris AP (2020b) Fault failure modes, deformation mechanisms, dilation tendency, slip tendency, and conduits versus seals. In *Integrated Fault Seal Analysis* (eds SR Ogilvie, SJ Dee, RW Wilson and WR Bailey), pp. 75–98. Geological Society of London, Special Publication no. 496.

Ferrill DA, Smart KJ and Morris AP (2020c) Resolved stress analysis, failure mode, and fault-controlled fluid conduits. *Solid Earth* **11**, 899–908.

Fisher QJ and Knipe RJ (2001) The permeability of faults within siliciclastic petroleum reservoirs of the North Sea and Norwegian Continental Shelf. *Marine and Petroleum Geology* **18**, 1063–81.

Foley LL (1926) Mechanics of the Balcones and Mexia faulting. *American Association of Petroleum Geologists Bulletin* **10**, 1261–9.

Gan Q and Elsworth D (2014) Analysis of fluid injection-induced fault reactivation and seismic slip in geothermal reservoirs. *Journal of Geophysical Research: Solid Earth* **119**, 3340–53.

Gasparrini M, Lacombe O, Rohais S, Belkacemi M and Euzen T (2021) Natural mineralized fractures from the Montney-Doig unconventional reservoirs (Western Canada sedimentary basin): timing and controlling factors. *Marine and Petroleum Geology* **124**, 104826.

Gautschi A (2001) Hydrogeology of a fractured shale (Opalinus Clay): implications for deep geological disposal of radioactive wastes. *Hydrogeology Journal* **9**, 97–107.

Gillespie PA, Johnston JD, Loriga MA, McCaffrey KLW, Walsh LL and Watterson L (1999) Influence of layering on vein systematics in line samples. In *Fractures, Fluid Flow and Mineralization* (eds KJW McCaffrey, L Lonergan and JJ Wilkinson), pp. 35–56. Geological Society of London, Special Publication no. 155.

Gillespie PA, Walsh JJ, Waterson J, Bonson CG and Manzocchi T (2001) Scaling relationships of joint and vein arrays from The Burren, Co. Clare, Ireland. *Journal of Structural Geology* **23**, 183–201.

Giorgetti C, Collettini C, Scuderi MM, Barchi MR and Tesei T (2016) Fault geometry and mechanics of marly carbonate multilayers: an integrated field and laboratory study from the Northern Apennines, Italy. *Journal of Structural Geology* **93**, 1–16.

Girardeau-Montaut D (2011) CloudCompare, a 3D point cloud and mesh processing free software. *Technical Report, EDF Research and Development, Telecom ParisTech*. http://www.danielgm.net/cc/ (accessed 13 January 2021).

Gross MR (1993) The origin and spacing of cross joints: examples from the Monterey Formation, Santa Barbara Coastline, California. *Journal of Structural Geology* **15**, 737–51.

Hancock PL (1985) Brittle microtectonics: principles and practice. *Journal of Structural Geology* **7**, 437–57.

Handin J, Hager Jr RV, Friedman M and Feather JN (1963) Experimental deformation of sedimentary rocks under confining pressure: pore pressure tests. *American Association of Petroleum Geologists Bulletin* **47**, 717–55.

Harris JF, Taylor GL and Walper JL (1960) Relation of deformational fractures in sedimentary rocks to regional and local structure. *American Association of Petroleum Geologists Bulletin* **44**, 1853–73.

Hooker JN and Katz RF (2015) Vein spacing in extending, layered rock: the effect of synkinematic cementation. *American Journal of Science* **315**, 557–88.

Hooker JN, Laubach SE and Marrett R (2013) Fracture-aperture size—frequency, spatial distribution, and growth processes in strata-bounded and non-strata-bounded fractures, Cambrian Mesón Group, NW Argentina. *Journal of Structural Geology* **54**, 54–71.

Hooker JN, Laubach SE and Marrett R (2014) A universal power-law scaling exponent for fracture apertures in sandstones. *Geological Society of America Bulletin* **126**, 1340–62.

Hovorka SD (1998) *Facies and Diagenesis of the Austin Chalk and Controls on Fracture Intensity: A Case Study from North-Central Texas.* Austin, Texas: The University of Texas at Austin, Bureau of Economic Geology, 47 pp.

Huang Q and Angelier J (1989) Fracture spacing and its relation to bed thickness. *Geological Magazine* **126**, 355–62.

James MR and Robson S (2012) Straightforward reconstruction of 3D surfaces and topography with a camera: accuracy and geoscience application. *Journal of Geophysical Research: Earth Surface* **117**, 1–17.

Katz O, Reches Z and Roegiers J-C (2000) Evaluation of mechanical rock properties using a Schmidt Hammer. *International Journal of Rock Mechanics and Mining Sciences* **37**, 723–8.

Ladeira FL and Price NJ (1981) Relationship between fracture spacing and bed thickness. *Journal of Structural Geology* **3**, 179–83.

Lamarche J, Lavenu APC, Gauthier BDM, Guglielmi Y and Jayet O (2012) Relationships between fracture patterns, geodynamics and mechanical stratigraphy in carbonates (South-East Basin, France). *Tectonophysics* **581**, 231–45.

Lattman LH and Parizek RR (1964) Relationship between fracture traces and the occurrence of ground water in carbonate rocks. *Journal of Hydrology* **2**, 73–91.

Laubach SE, Lamarche J, Gauthier BDM, Dunne WM and Sanderson DJ (2018) Spatial arrangement of faults and opening-mode fractures. *Journal of Structural Geology* **108**, 2–15.

Laubach SE, Olson JE and Gross MR (2009) Mechanical and fracture stratigraphy. *American Association of Petroleum Geologists Bulletin* **93**, 1413–26.

Ledbetter Ferrill NS and Ferrill DA (2021) Influence of mechanical layering and natural fractures on undercutting and rapid headward erosion (recession) at Canyon Lake spillway, Texas, USA. *Engineering Geology* **280**, 1–13.

Li JZ, Laubach SE, Gale JFW and Marrett RA (2018) Quantifying opening-mode fracture spatial organization in horizontal wellbore image logs, core and outcrop: application to upper Cretaceous Frontier Formation tight gas sandstones, USA. *Journal of Structural Geology* **108**, 137–56.

Lorenz JC, Sterling JL, Schechter DS, Whigham CL and Jensen JL (2002) Natural fractures in the Spraberry Formation, Midland Basin, Texas: the effects of mechanical stratigraphy on fracture variability and reservoir behavior. *American Association of Petroleum Geologists Bulletin* **86**, 505–24.

McGinnis RN, Ferrill DA, Morris AP, Smart KJ and Lehrmann D (2017) Mechanical stratigraphic controls on natural fracture spacing and penetration. *Journal of Structural Geology* **95**, 160–70.

McGinnis RN, Ferrill DA, Smart KJ, Morris AP, Higuera-Diaz C and Prawica D (2015) Pitfalls of using entrenched fracture relationships: fractures in bedded carbonates of the Hidden Valley Fault Zone, Canyon Lake Gorge, Comal County, Texas. *American Association of Petroleum Geologists Bulletin* **99**, 2221–45.

McQuillan H (1973) Small-scale fracture density in Asmari Formation of Southwest Iran and its relation to bed thickness and structural setting. *American Association of Petroleum Geologists Bulletin* **57**, 2367–85.

Morris AP, Ferrill DA and McGinnis RN (2009a) Fault frequency and strain. *Lithosphere* **1**, 105–9.

Morris AP, Ferrill DA and McGinnis RN (2009b) Mechanical stratigraphy and faulting in Cretaceous carbonates. *American Association of Petroleum Geologists Bulletin* **93**, 1459–70.

Morris AP, Ferrill DA and McGinnis RN (2016) Using fault displacement and slip tendency to estimate stress states. *Journal of Structural Geology* **83**, 60–72.

Morris AP, McGinnis RN and Ferrill DA (2014) Fault displacement gradients on normal faults and associated deformation. *American Association of Petroleum Geologists Bulletin* **98**, 1161–84.

Murray GE (1961) *Geology of the Atlantic and Gulf Coastal Province of North America.* New York: Harper and Brothers, 692 pp.

Na S, Sun W, Ingraham MD and Yoon H (2017) Effects of spatial heterogeneity and material anisotropy on the fracture pattern and macroscopic effective toughness of Mancos Shale in Brazilian tests. *Journal of Geophysical Research: Solid Earth* **122**, 6202–30.

Narr W and Suppe J (1991) Joint spacing in sedimentary rocks. *Journal of Structural Geology* **13**, 1037–48.

Nelson RA (2001) *Geologic Analysis of Naturally Fractured Reservoirs.* Boston: Gulf Professional Publishing, 332 pp.

Olson JE (2004) Predicting fracture swarms—the influence of subcritical crack growth and the cracktip process zone on joint spacing in rock. In *The Initiation, Propagation, and Arrest of Joints and Other Fractures* (eds T Engelder and JW Cosgrove), pp. 73–87. Geological Society of London, Special Publication no. 231.

Price NJ (1966) *Fault and Joint Development in Brittle and Semi-Brittle Rock.* London, UK: Pergamon Press, 176 pp.

Rawnsley K, De Keijzer M, Wei L, Bettembourg S, Asyee W, Massaferro JL, Swaby P, Drysdale D and Boettcher D (2007) Characterizing fracture and matrix heterogeneities in folded Devonian carbonate thrust sheets, Waterton tight gas fields, Western Canada. In *Fractured Reservoirs* (eds L Lonergan, RJH Jolly, K Rawnsley and DJ Sanderson), pp. 265–79. Geological Society of London, Special Publication no. 270.

Rijken P and Cooke ML (2001) Role of shale thickness on vertical connectivity of fractures: application of crack-bridging theory to the Austin Chalk, Texas. *Tectonophysics* **337**, 117–33.

Roche V, Homberg C and Rocher M (2012) Fault displacement profiles in multilayer systems: from fault restriction to fault propagation. *Terra Nova* **24**, 499–504.

Roche V and van der Baan M (2013) The role of lithological layering on spatial variation of natural and induced fractures in hydraulic fracture stimulation. *American Association of Petroleum Geologists Search and Discovery Article* **90187**, 1–4.

Schultz RA (2000) Growth of geologic fractures into large-strain populations: review of nomenclature, subcritical crack growth, and some implications for rock engineering. *International Journal of Rock Mechanics and Mining Sciences* **37**, 403–11.

Solum JG and Huisman BAH (2017) Toward the creation of models to predict static and dynamic fault-seal potential in carbonates. *Petroleum Geoscience* **23**, 70–91.

Stearns DW and Friedman M (1972) Reservoirs in fractured rock: geologic exploration methods. In *Stratigraphic Oil and Gas Fields* (ed. HR Gould), pp. 82–106. American Association of Petroleum Geologists Memoir no. 16.

Stowell JFW (2001) Characterization of opening-mode fracture systems in the Austin Chalk. *Gulf Coast Association of Geological Societies Transactions* **51**, 313–20.

Thiele ST, Grose L, Samsu A, Micklethwaite S, Vollgger SA and Cruden AR (2017) Rapid, semi-automatic fracture and contact mapping for point clouds, images and geophysical data. *Solid Earth* **8**, 1241–53.

Vialle S, Ajo-Franklin J and Carey JW (2018) *Geological Carbon Storage: Subsurface Seals and Caprock Integrity.* Hoboken, New Jersey: John Wiley & Sons Inc., 352 pp.

Ward WC and Ward WB (2007) Stratigraphy of the middle part of Glen Rose Formation (Lower Albian), Canyon Lake Gorge, central Texas. In *Cretaceous Rudists and Carbonate Platforms: Environmental Feedback* (ed. RW Scott), pp. 193–210. SEPM Special Publication no. 87.

Worthington MH and Lubbe R (2007) The scaling of fracture compliance. In *Fractured Reservoirs* (eds L Lonergan, RJH Jolly, K Rawnsley and DJ Sanderson), pp. 73–82. Geological Society of London, Special Publication no. 270.

Wu H and Pollard DD (1991) Fracture spacing, density, and distribution in layered rock masses: results from a new experimental technique. In *Rock Mechanics as a Multidisciplinary Science: Proceedings of the 32nd US Symposium* (ed. J-C Roegiers), pp. 1175–84. Rotterdam: A. A. Balkema.

Yielding G, Needham T and Jones H (1996) Sampling of fault populations using sub-surface data: a review. *Journal of Structural Geology* **18**, 135–46.

Yin HM (2010) Fracture saturation and critical thickness in layered materials. *International Journal of Solids and Structures* **47**, 1007–15.

Young K (1972) Mesozoic history, Llano region. In *Geology of the Llano Region and Austin Area, Field Excursion* (eds VE Barnes, WC Bell, SE Clabaugh, PE Cloud Jr, RV McGehee, PU Rodda and K Young), pp. 41–6. Austin, Texas: University of Texas at Austin, Bureau of Economic Geology Guidebook 13.

Zahm CK and Hennings PH (2009) Complex fracture development related to stratigraphic architecture: challenges for structural deformation prediction, Tensleep Sandstone at the Alcova anticline, Wyoming. *American Association of Petroleum Geologists Bulletin* **93**, 1427–46.